**Title**
Investigation of Nb3Sn Based Superconductors Through Hierarchical Models



**Author**
Collins, Brett

**Publication Date**
2013

Peer reviewed|Thesis/dissertation

# Investigation of $Nb_3Sn$ Based Superconductors Through Hierarchical Models

by

Brett Charles Collins

A dissertation submitted in partial satisfaction of the
requirements for the degree of
Doctor of Philosophy

in

Engineering - Mechanical Engineering

in the

GRADUATE DIVISION
of the
UNIVERSITY OF CALIFORNIA, BERKELEY

Committee in charge:

Professor Tarek I. Zohdi, Chair
Professor David J. Steigmann
Professor Per-Olof Persson

Spring 2013

**Investigation of $Nb_3Sn$ Based Superconductors Through Hierarchical Models**

## Abstract

Investigation of $Nb_3Sn$ Based Superconductors Through Hierarchical Models

by

Brett Charles Collins
Doctor of Philosophy in Engineering - Mechanical Engineering

University of California, Berkeley

Professor Tarek I. Zohdi, Chair, Chair

The large range of length scales present within accelerator magnets suggests the incorporation of a hierarchical structure into computational models. Evaluation of the strain state present within the superconducting filaments is necessary in order to determine the critical current of $Nb_3Sn$ based magnets. As part of an ongoing investigation at LBNL, a three-dimensional nonlinear multiscale model is developed to investigate the behavior of $Nb_3Sn$ filaments due to macroscopic loading. The major building blocks within a superconducting magnet are used to represent each length scale within the multiscale model: Coil, Rutherford cable, strand, filament, $Nb_3Sn$ crystal lattice. Using the developed model, loads at the coil level due to precompression, thermal contraction, and Lorenz forces are translated into lattice strain within the $Nb_3Sn$ phase of the composite. $J_c$ can then be calculated through use of measurements performed on bulk samples of $Nb_3Sn$. In addition, the physical effects on each scale due to loading is examined. Each level of the hierarchical model is solved using Finite Element Methods, taking into account effects due to thermal contraction and plasticity. A conjugate gradient algorithm is coupled with a Netwon's method with line search in order to solve resulting systems of equations.

Professor Tarek I. Zohdi, Chair, Chair

I dedicate this dissertation to my parents. Without their unwavering support and love, I wouldn't be the person I am today.

# Contents

## Acknowledgments

I would like to express my deep appreciation to my committee chair and advisor, Professor Tarek Zohdi, for his guidance during the course of this research. In addition to welcoming me into his lab and providing me with the opportunity to participate in this project, he was also a constant source of ideas.

I would also like to thank my committee members, Professor David Steigmann and Professor Per-Olof Persson, for their advice on my dissertation and course work.

In addition, I would like to express my gratitude to the Supercon group at Lawrence Berkeley National Laboratory for providing this research topic. I want to thank Paolo Ferracin, Soren Prestemon, and Diego Arbelaez for their persistent help and feedback on the project.

Thank you to the Department of Energy Office of Science for allowing me to participate in the Office of Science Graduate Fellowship program. In addition to being very beneficial to my project, having the opportunity to learn about the research currently being performed across the country has expanded my horizons.

Thanks as well to my family and friends for their consistent support and encouragement throughout the years.

Finally, I want to thank Paulina Rabczak, who has been with me since day one. There are no words that can accurately convey my gratitude towards her for all that she's done for me. Without her vigilant support and gentle prodding, I'd still be writing this dissertation.

# Chapter 1

# Introduction

Ideally, in order to reduce laboratory expensess, predictions for the complex behaviors of superconducting magnets can be made through numerical simulations. With the computational power currently available for mathematical modeling and simulation, modern numerical methods can play a significant role in the analysis of superconducting magnets. The primary objective of this dissertation is to develop a numerical framework to model the applications of superconducting magnets, with emphasis on accelerator magnets.

The ability to obtain a three dimensional strain state in $Nb_3Sn$ filaments due to macro-scale loading is vital in determining the critical current carrying capacity of an accelerator magnet. However, this task is not trivial due to the variety of important length scales present in superconducting magnets: magnet, coil, cable, strand, filaments, and lattice. These scales, shown in detail in 1.1, each play an important role in the final strain state present in the filaments. Direct numerical simulation of the macro-scale magnet with the inclusion of all the micro-scale details is computationally infeasible. Therefore, multi-scale computation can be used to understand the behavior across various length scales. Due to the vast difference in these length scales, multiple models must be created to accurately incorporate the physics present at each scale. In the present work, the main focus is on the development of models that bridge the strand and filament scales in a rod restack process (RRP) strand.

The numerical determination fo the strain stae present in $Nb_3Sn$ filaments has previously been explored. Mitchell [55] has developed one and two dimensional models to simulate thermo-mechanical loads on strands to determine the corresponding strain state in $Nb_3Sn$ filaments. Meanwhile, Boso [12] [13] has developed a multiscale model to examine the strain state in $Nb_3Sn$ based strands for ITER coils. Arbelaez [20] has developed a multiscale model bridging the strand and cable levels in order to determine the effective linear, orthotropic properties of Rutherford cables. Chen [41] has developed an elastic model to characterize the strain of $Nb_3Sn$ filaments in a wire.

In the present study, a multiscale model is developed and used to examine the

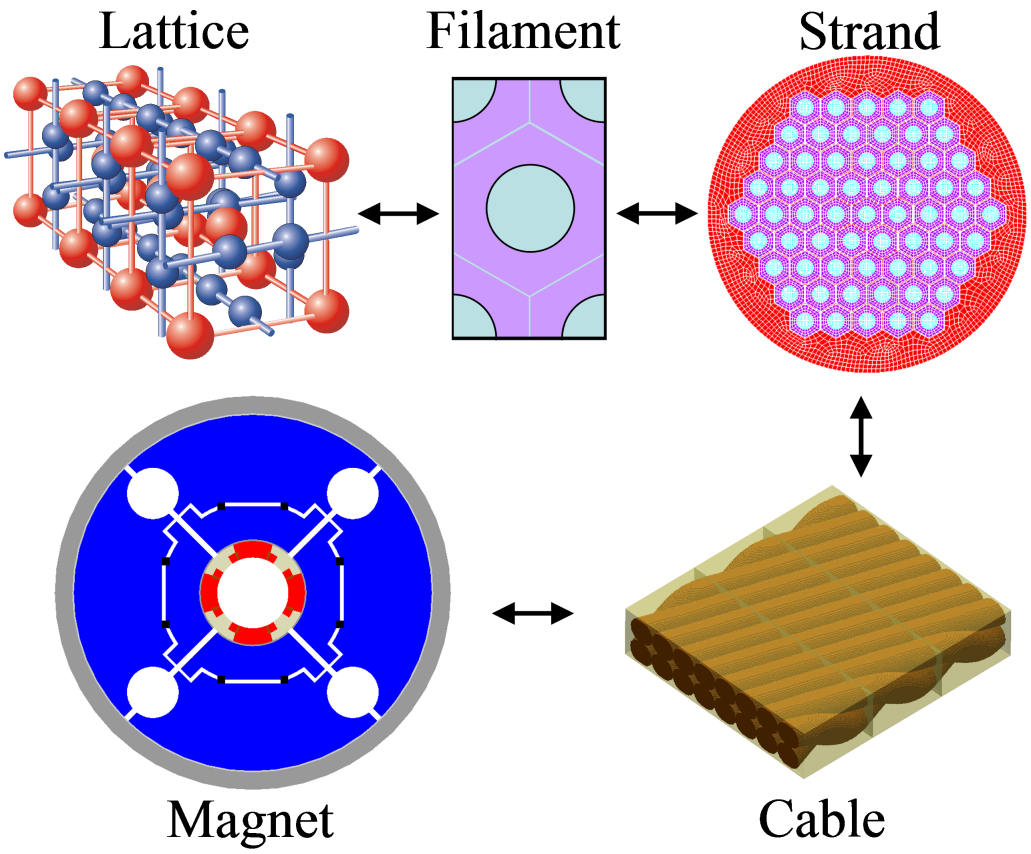


Figure 1.1: Illustration of the scales present in $Nb_3Sn$ magnets: magnet, cable, strand, filaments, lattice.

relation between the strand and filmanet scales. As discovered previously [9], the copper portion of a strand exhibits plasticity, and therefore work hardening, simply from cooling the system down from room temperature to an operating temperature of 4.2 K. Therefore, it is necessary that a nonlinear material model is included in the problem formulation.

The organization of this dissertation is as follows. In chaper 2, the basics of superconducting accelerator magnets is discussed. In chapter 3, the governing equations representing the underlying physics within an accelerator magnet, as well as the material models present within the system, are examined. In chapter 4, the numerical methods used to solve the partial differential equations discussed in chapter 3 are developed, with particular attention to the finite element method. In chapter 5, the implementation of a multiscale model is discussed. In chapter 6, the multiscale model is applied to a superconducting RRP strand and three test cases are examined.

# Chapter 2

# The Basics of Superconducting Accelerator Magnets

## 2.1 History of Superconductivity

Superconductivity is a phenomenon in which certain materials possess the property of zero electrical resistance. The discovery of superconductivity is closely linked with the development of cryogenics in the late 1800s. Dutch scientist Kamerlingh Onnes performed research on the resistivity of materials at cryogenic temperatures in 1911, where electrical resistivity is defined as

$$\rho = R\frac{A}{l} \tag{2.1}$$

where $R$ is the electrical resistance of a uniform specimen of material, $l$ is the length of the specimen, and $A$ is the cross-sectional area of the specimen. The resistivity of platinum and gold were observed to decrease steadily to a constant value as temperature decreased, as shown in figure 2.1 [63]. However, the resistivity of mercury dropped to an imperceptibly low value at a temperature below $4.2K$. Upon repeating the measurement with greater sensitivity, it was observed that the drop to zero resistivity occured abruptly, just below the boiling point of helium, as shown in figure 2.2 [14]. Soon after, superconductivity had been found in numerous other elements and alloys.

## 2.2 Particle Accelerators

A particle accelerator is a device that uses electromagnetic fields to propel charged particles to high speeds and to contain them in well-defined beams [49]. In a circular accelerator, particles move in a circle until they reach a sufficient energy level, at which their interactions can be observed in high energy collisions. One of these

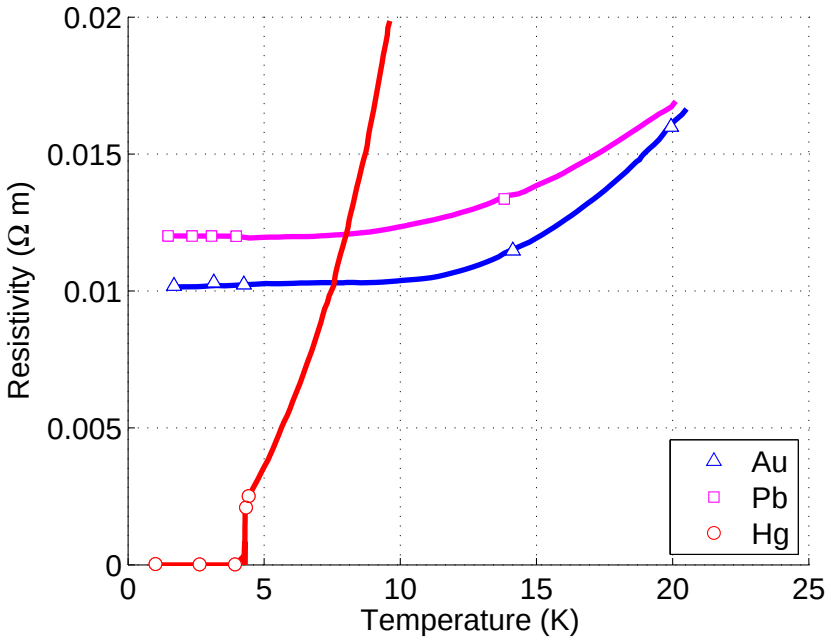


Figure 2.1: Resistivity vs. Temperature. for Gold, Platinum, and Mercury

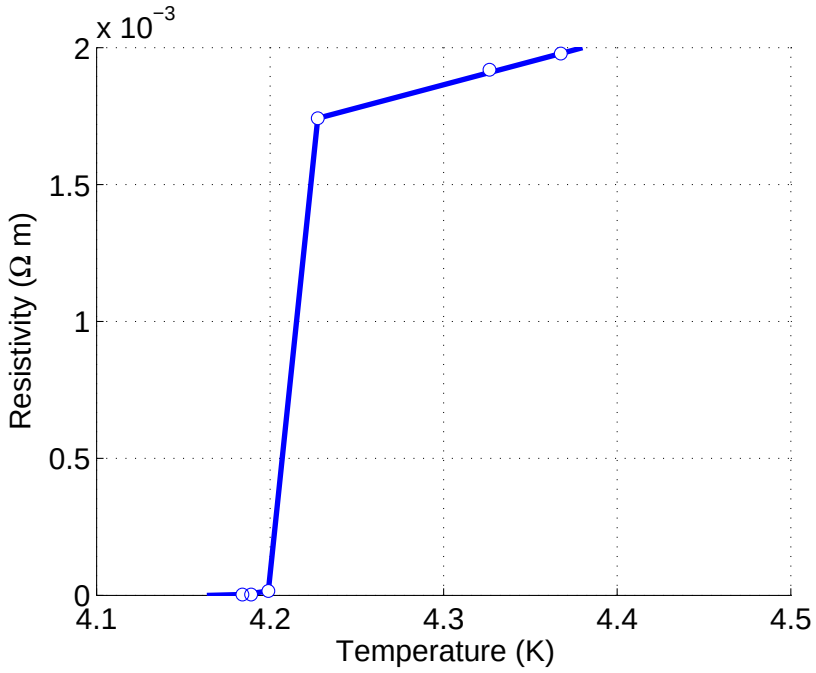


Figure 2.2: Resistivity of Mercury vs. Temperature - Zoomed.

particle accelerators, the Large Hadron Collider (LHC), can be seen in figure 2.3. The particle trajectories are bent into a circle using electromagnets, using dipole magnets (two magnet coils) to bend the beam, and quadrupoles (four magnet coils) to focus the beam. A cross-section of the quadrupole used in the LHC can be seen in figure 2.4.

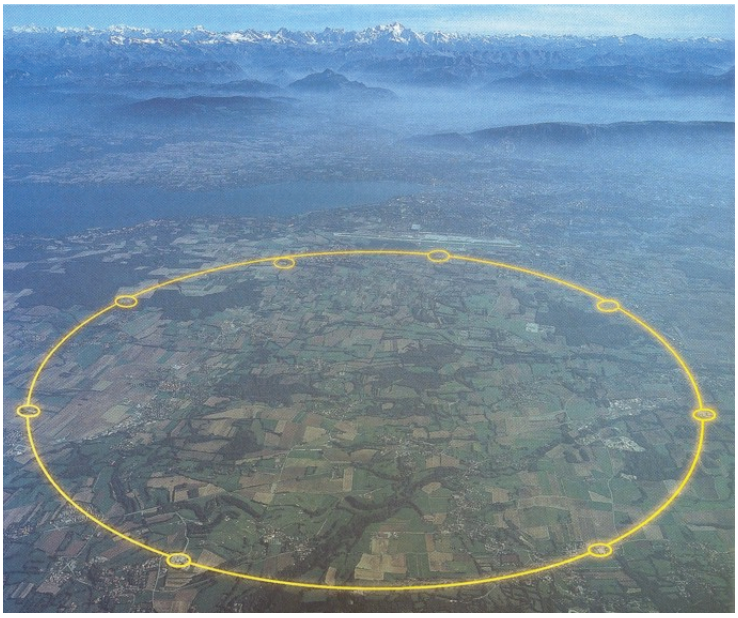

Figure 2.3: Overhead View of the Large Hadron Collider.

## 2.3 Critical Temperature, Critical Field and Critical Current

When a superconductor is cooled below a material specfic critical temperature, $T_c$, its restance abruptly drops to zero and it becomes the perfect electrical conductor. To show that the electrical resistance of a superconducting sample was in fact zero and not simply within the sensitivity limit of the measuring equipment, in 1914 Onnes created an electric current flowing in a closed superconducting ring [64]. A decay in electrical current was not observed, indicating that energy was not being transformed into Joule heat and therefore that the resistance of the material was exactly zero.

In the precesence of an applied magnetic field **H**, two types of superconductors are observed. These superconductors are generally classified as Type I and Type II. In a Type I superconductor, interior of a bulk superconductor cannot be penetrated by a weak magnetic field, a phenomenom known as the Meissner effect, which can be

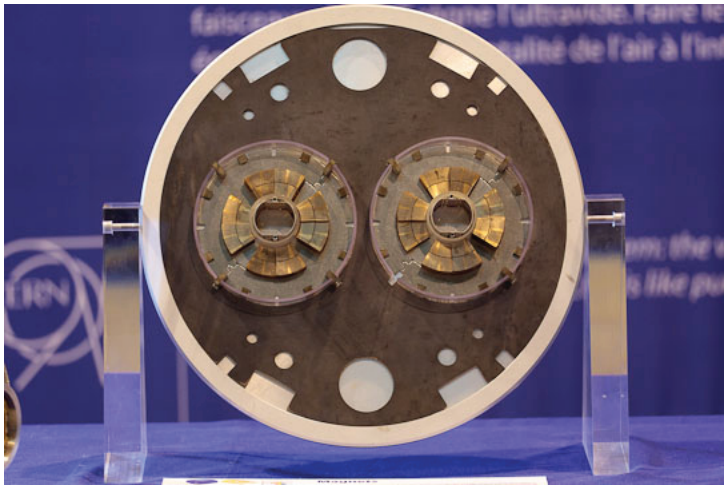

Figure 2.4: Quadrupole used in the Large Hadron Collider.

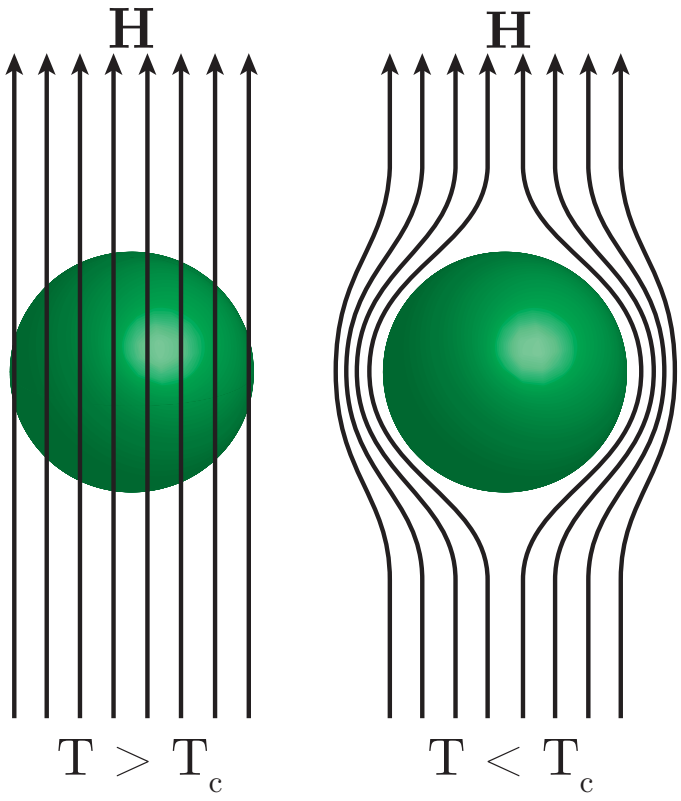


Figure 2.5: Expulsion of Magnetic Field in Superconductors.

seen in figure 2.5. The magnetic flux, **B** is completely shielded from the interior of the superconductor by shielding currents along its surface up until a critical magnetic field $H_c$. Type I superconductors have limited practical usefulness because the critical magnetic fields are small and there is an abrupt change from superconducting state. This can be visualized in figure 2.6.

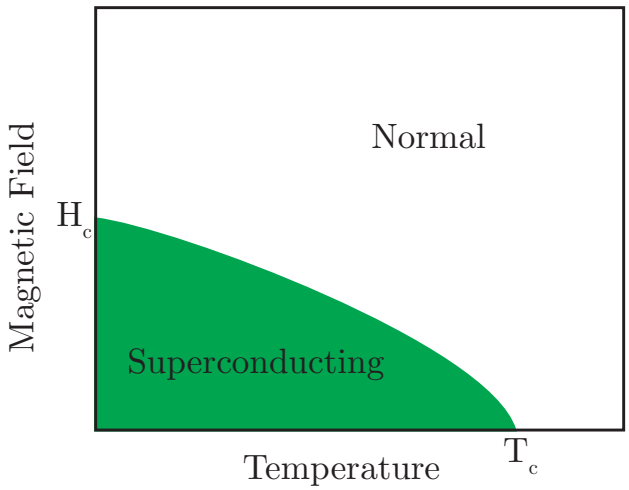


Figure 2.6: Applied Magnetic Field vs. Temperature for a Type I Superconductor.

Type II superconductors, which are made from alloys, have two critical fields, $H_{c1}$ and $H_{c2}$. At applied fields below $H_{c1}$, Type II superconductors exhibit the same perfect magnetic flux exclusion as Type I superconductors. Above $H_{c1}$ and below $H_{c2}$, magnetic flux penetrates the interior in the form of quantized flux vortices, or flux-lines, and the material exists in a mixed state of normal and superconducting regions [2], shown in figure 2.7. As the applied magnetic field increases from $H_{c1}$ to $H_{c2}$, the flux-line density increases from zero until they start to overlap and the superconductor undergoes a phase transition to the normal state. Due to their much higher critical magnetic fields, Type II superconductors are preferred in practical settings.

If a current flows through an ideal Type II superconductor which is exposed to a magnetic field, the current exerts a Lorentz force on the flux lines and causes them to move through the specimen in a direction perpendicular to the current and field. This can be seen in figure 2.8, where **B** is the macroscopic magnetic field, **J** is the current density, and **v** is the flux-line velocity. The macroscopic magnetic field is defined as

$$\mathbf{B} = \mu_0 \left( \mathbf{H} + \mathbf{M} \right) \tag{2.2}$$

where $\mu_0$ is the permeability of free space constant and **M** is the superconductor magnetization. This is a viscous motion that generates a potential gradient, i.e.

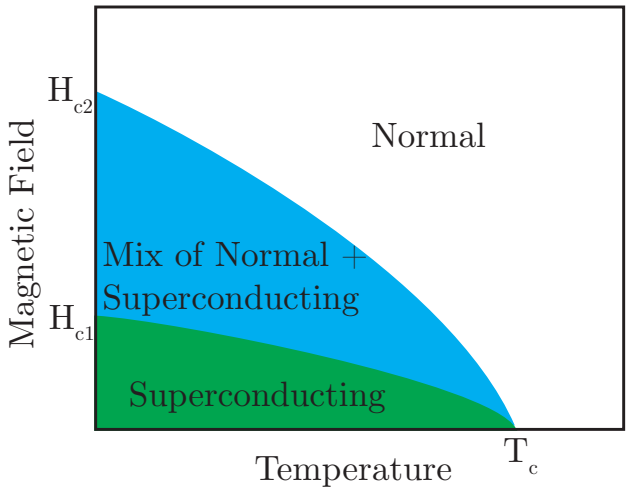


Figure 2.7: Applied Magnetic Field vs. Temperature for a Type II Superconductor.

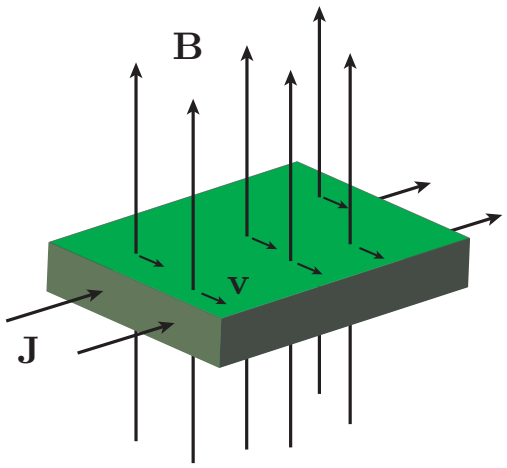


Figure 2.8: Scheme of Fluxoid Motion in a Current-Carrying Type II Superconductor.

voltage, which leads to heat generation and therefore destroys the superconducting state. However, the flux-line lattice can be "pinned" by lattice imperfections such as impurities, precipitation of other material phases, grain boundaries, or defects. A critical current density $J_c$ is defined to be when the Lorrentz force acting on the flux-line lattice becomes larger than the bulk pinning force $F_p$, which prevents the flux-lines from moving [43]. The pinning force, and therefore $J_c$, depends on the applied field and temperature and can be written as $J_c(H, T)$. This function represents a critical surface bounding the superconducting region, and can be visualized in figure 2.9.

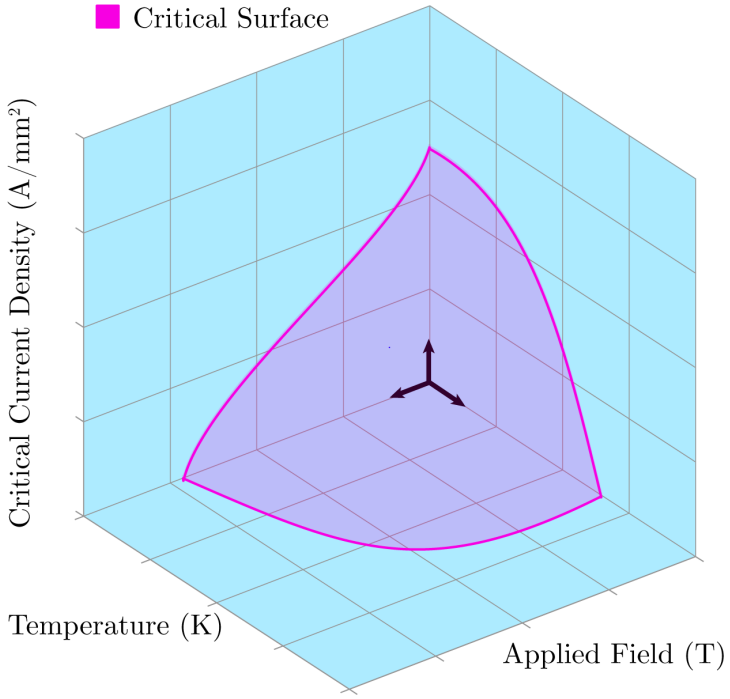


Figure 2.9: Critical Surface Bounding the Superconducting Region.

## 2.4 Relevant Superconducting Materials

A wide variety of metals and alloys display superconductivity, however, only two are commercially available for large scale magnet production: niobium-titanium, NbTi, and niobium-tin, $Nb_3Sn$ [54]. Typical critical current densities achieved are plotted in figure 2.10 as a function of field [46].

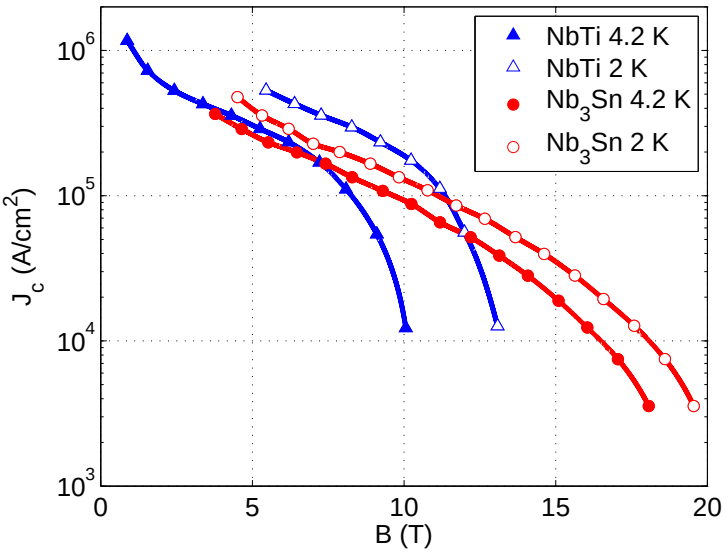


Figure 2.10: Critical Current Density as a Function of Magnetic Field.

### 2.4.1 NbTi

The most widely used superconductor is the ductile alloy NbTi [48] [27] [85]. Niobium and titanium have similar atomic sizes, with a difference in radii of approximately 5 pm, and are mutually soluable over a wide composition range [11]. At high temperatures, they form a body-centered cubic phased alloy. When cooled down to below approximately $9.2K$, this alloy becomes superconducting. $\mu_0 H_{c2}$ is approximately 14.5 T at 0 K and approximately 10 T at 4.2 K [34].

Within the NbTi alloy, large amounts of lattice dislocations and well as precipitations of other phases at grain boundaries are present, which have shown to be very efficient in pinning the fluxoids present in the mixed state of Type II superconductors [47] [53].

One of the most significant features of NbTi is its extreme ductility, which allows simple and effective fabrication methods for wires and cables, such as extrusion and drawing. For this reason, NbTi is widely used in magnets with field strengths up to 6.5 T. The Tevatron accelertor in Fermilab was the first project where NbTi was implemented on a large scale, and many other particle accelerators have followed since [16] [82] [8] [28]. The primary application of NbTi wires today is the manufactoring of full-body Magnetic Resonance Imaging (MRI) magnets [56].

### 2.4.2 $Nb_3Sn$

The alternative superconducting material that is readily available is the compound $Nb_3Sn$. Niobium-tin is a brittle intermetallic compound of well-defined stoichiometry which crystallizes in the so-called A15 lattice [48] [27] [85]. The Sn atoms form a body-centered cubic lattice, and each face is bisected by orthogonal Nb chains, shown in figure 2.11. $T_c$ is approximately 18 K and $\mu_0 H_{c2}$ is approximately 25 T for this alloy [56] [65] [29].

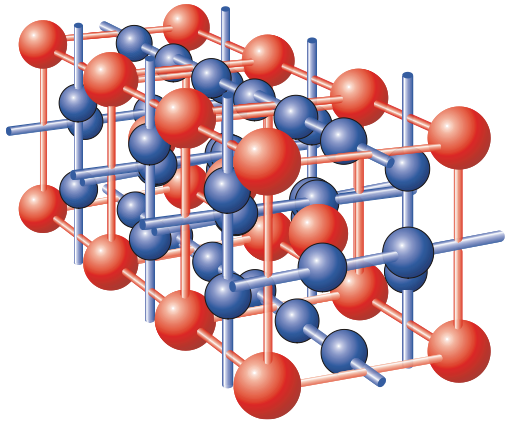

Figure 2.11: Schematic of the $Nb_3Sn$ A15 unit lattice, with red spheres representing Sn atoms and blue spheres representing Nb atoms.

Similarly to other A15 compounds, the main sources of fluxoid pinning sites in $Nb_3Sn$ are at the grain boundaries. The alloy must therefore be processed to achieve fine, homogeneous microstructure with grain diameters between 30 and 300 nm to achieve a high critical current [67].

The main drawbacks to $Nb_3Sn$ as a superconductor are its brittleness and its sensitivity to strain [57] [5] [17]. Due to its brittle nature, it is much more cumbersome to effectively fabricate $Nb_3Sn$ wires and cables. As opposed to NbTi, A15 superconductors cannot be drawn into thin filaments, but instead must be formed in the final geometry by high temperature heat treatment. $Nb_3Sn$, for example, needs to undergo reaction at $650 - 700\ ^\circ C$ for many days to achieve full performance [54].

### 2.4.3 The Effect of Strain on Critical Current

The superconducting properties of all materials are sensitive to lattice strain to a certain extent, although the effect is small in NbTi. In NbTi, $J_c$ is primarily determined by the alloy microstructure, and can be optimized through applications of cold-work cycles and heat treatments. In $Nb_3Sn$, like other A15 compounds, $H_c$, $T_c$ and $J_c$ are affected by the lattice strain, and therefore mechanical stress. The

effect of uni-axial stress on the upper critical magnetic can be seen in figure 2.12 [17] and the effect of uni-axial stress on normalized critical current can be seen in figure 2.13 [19]. It can be seen that the presence of lattice strain severely degrades

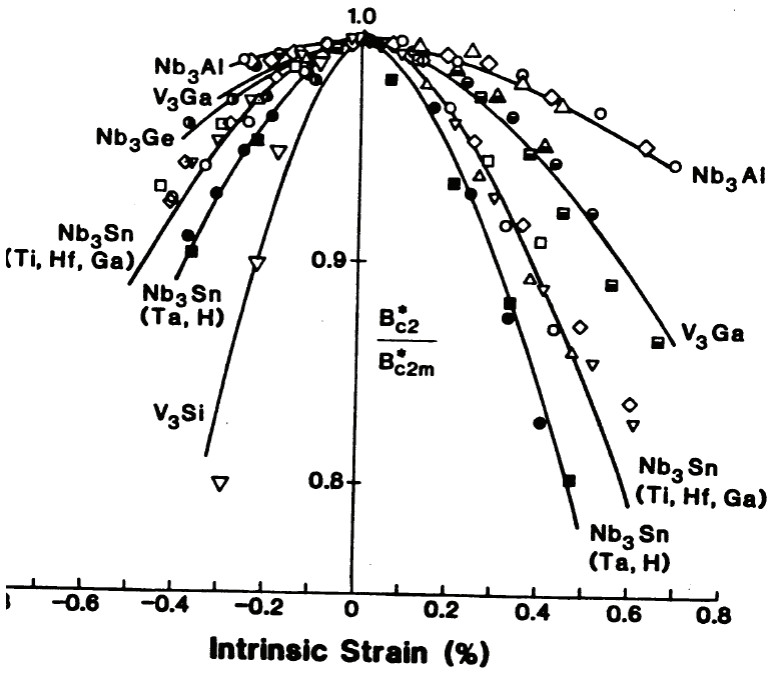


Figure 2.12: Effect of uniaxial strain on the upper critical field of practical A15 superconductors.

the critical properties of A15 superconductors. Therefore, accelerator magnets using $Nb_3Sn$ cannot be wound from the fully reacted cables due to the resulting bending strains.

## 2.5 Quenching

A quench is a termination of magnet operation in which the superconducting material returns to a resistive state. This can occur due to large magnetic fields that result in eddy currents, defects in the magnet that result in Joule heating, or improper cooling of the magnet. Local quenches often result in a chain reaction throughout the magnet, rapidly causing the entire coil to enter a resistive state. Quenches can often lead catostrophic damages to the magnet. Therefore, quench protection is often built into the system.

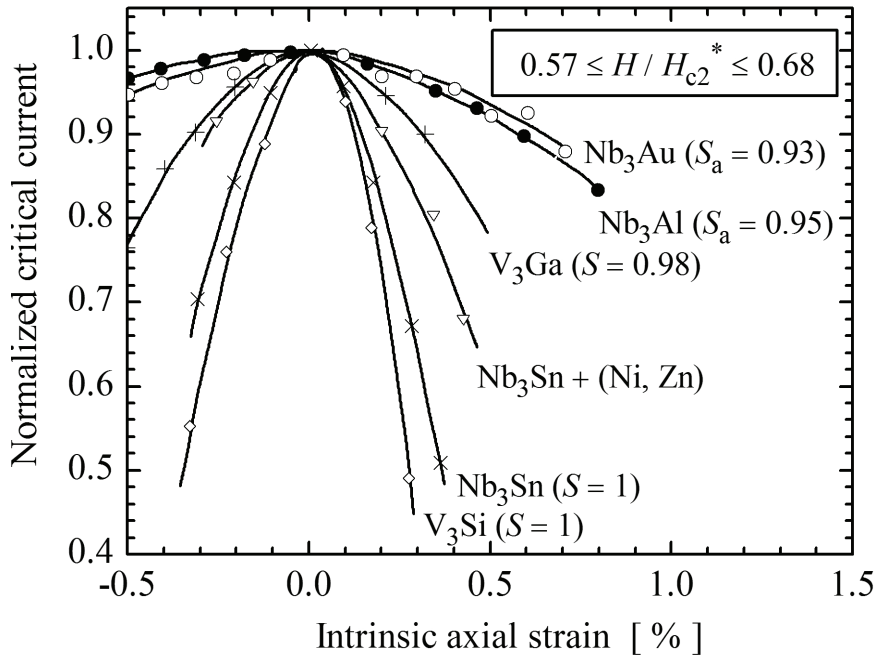


Figure 2.13: Effect of uniaxial strain on the critical current density of practical A15 superconductors.

## 2.6 Multifilament Superconductors

### 2.6.1 Overview

In practical applications, superconductors are subdivided into fine filaments, which are twisted together and embedded within a normal metal with low resistivity, such as copper. This can be visulized in figure 2.14, where the smaller filaments are NbTi and the matrix is Cu. This composite is referred to as a strand.

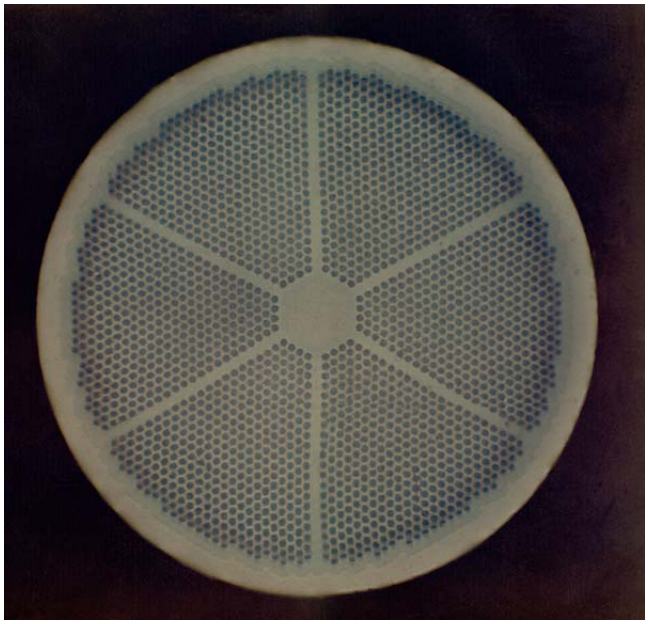

Figure 2.14: Cross Section of Superconducting Wire (Courtesy of Fermilab Visual Media Services).

Having small filaments is necessary in a a practical superconductor in order to eliminate instabilities known as flux jumps [84]. These flux jumps are caused by thermal perturbations that arise in type-II superconductors, and are more likely to arise in bulky superconductors than subdivided ones. There exist numerous methods developed to estimate critical filament diameters, such as the adiabatic stability criterion and the dynamic stability criterion. In the adiabity stability criterion, a slab of thickness $2d_{\text{slab}}$ is considered alone in free space. Assuming adiabitic conditions, it can be shown that a necessary condition to prevent the flux jump instability is $d_{c,\text{adiabatic}} < d_{\text{slab}}$, where

$$d_{c,\text{adiabatic}} = \sqrt{\frac{3C_{sc}\left(T_0, B_0\right)}{\mu_0 J_c\left(T_0, B_0\right)\left|\frac{\partial J_c}{\partial T}\left(T_0, B_0\right)\right|}}, \tag{2.3}$$

where $C_{sc}$ is the superconductor specific heat per unit volume.

The dynamic criterion considers composite wire with a circular cross section made up of superconducting filaments of diameter $d_{\text{filament}}$ in a normal metal matrix. The necessary condition to prevent the flux jump instability is $d_{c,\text{dynamic}} < d_{\text{filament}}$, where

$$d_{c,\text{dynamic}} = \sqrt{\frac{32\lambda_{wire}k_{sc}\left(T_0, B_0\right)}{\rho_{matrix}J_c\left(RRR, T_0, B_0\right)J_c\left(T_0, B_0\right)\left|\frac{\partial J_c}{\partial T}\left(T_0, B_0\right)\right|}}, \tag{2.4}$$

where $\lambda_{\text{wire}}$ is the matrix to superconductor ratio, $k_{sc}$ is the thermal conductivity of the superconductor, $\rho_{\text{matrix}}$ is the resistivity of the matrix, and $RRR$ is the residual resistivity ratio of the matrix. It can be seen that $d_c$ is inversly proportional to $J_c$, implying that for larger critical currents, smaller superconducting filaments are required to prevent flux jump instabilities.

Within a strand whose filaments are straight, eddy currents are induced when subjected to a time-varying magnetic flux due to the low resistivity matrix. A schematic of this process is shown in figure 2.15. Twisting filaments reduces the chance of filament coupling by limiting the induction loop for the coupling current from the length of the conductor to a half of the twist pitch [87].

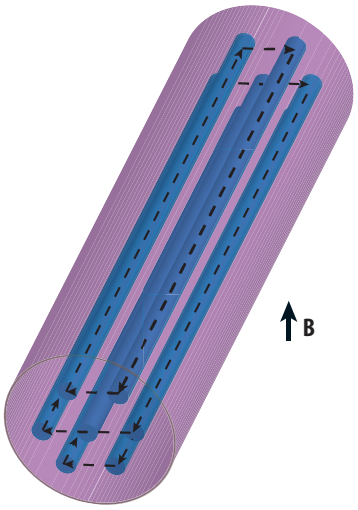


Figure 2.15: Interfilament coupling within an untwisted superconducting wire subjected to an applied magnetic field.

A low resistivity matrix is used to limit power dissipation due to Joule heating in the case of the transition of superconducting filaments to normal conducting filaments. In the event of a quench, if the resistance of the matrix material is sufficiently low, there is enough time to shut the system down to prevent permanent damage to the magnet.

### 2.6.2 Wire Fabrication

In the fabrication process of a wire, the separate components are stacked in billets and then extruded/drawn into wires. Since the A15 phase is brittle, the wires must be drawn while the components are net yet reacted so that they remain ductile. The A15 formation reaction occurs after wires are drawn into their final dimensions, and after coil winding. The A15 reaction occurs at approximately 950 K in a protected atmoshphere through a solid state diffusion reaction over the course of 10-15 days. An example heat treatment of a wound superconducting coil can be seen in figure 2.16.

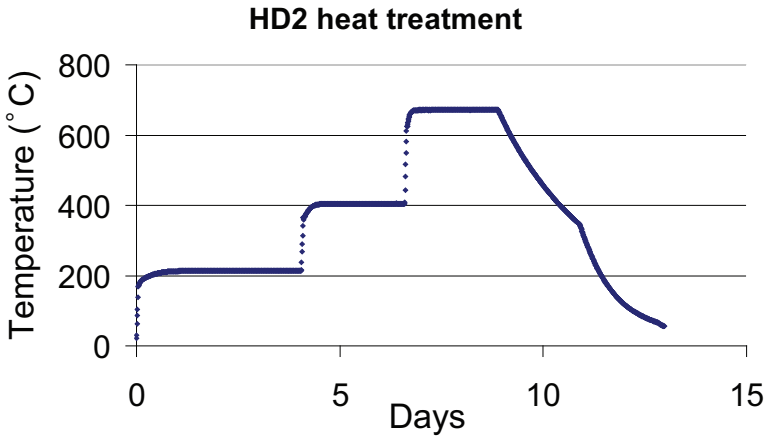


Figure 2.16: Heat Treatment of a Superconducitng Coil.

The three present large scale fabrication processes are the bronze process [4], powder-in-tube process [42], and the internal Sn process [86]. Although all three fabrication processes have benefits and drawbacks, the primary one considered in this work will be the internal Sn process, which can be visualized in figure 2.17.

In the internal Tin process, a Sn core srounded by Nb rods embedded withiin Cu (known as the Rod Restack Process (RRP)). These filamentary regions are surrounded by a Sn diffusion barrier, typically composed of either Nb or Ta. One advantage of the internal Sn process is that it exhibits a larger Sn to Cu ratio than other fabrication processes, resulting in high Sn A15 layers and removing the need for intermediate annealing steps. The drawback is that the Sn core region does not become an A15 area during the reaction process [19].

### 2.6.3 Rutherford Cables

A Rutherford cable is made up strands, twisted together, and shaped into a flat, two-layer cable [85] [69], shown in figure 2.18. This type of cable was developed at

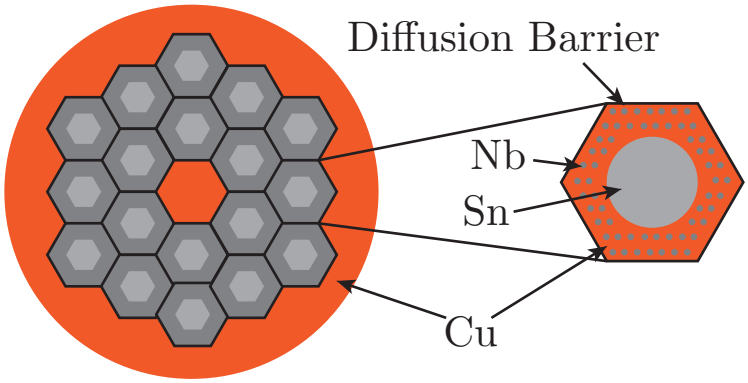


Figure 2.17: Schematic of the internal Sn process.

the Rutherford Appleton Laboratory [75], and the main benefit is that it allows for ease of stacking. It is often given a keystone-shape to allow stacking into an arch, which is useful for accelerator magnet coils.

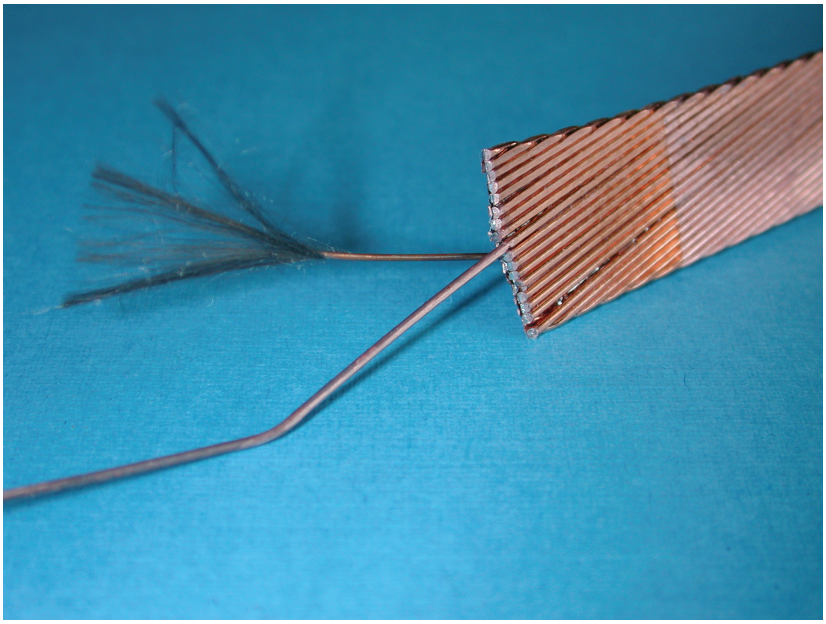

Figure 2.18: Rutherford Cable.

# Chapter 3

# Governing Equations and Material Models

A variety of physics are present during the operation of an accelerator magnet. These include electromagnetic phenomena due to using current to generate a magnetic field as well as accelerating a charged particle within a magnetic field, thermodynamic considerations when using cryogenics to cool the system to operating temperature, fluid mechanics within the liquid helium used to cool the system, and solid mechanics within the body of the accelerator magnet. The formulations behind these physical phenomena are discussed in this chapter, and the numerical implementations are discussed in later chapters.

## 3.1 Electromagnetics

Although the effects of electromagnetism are critical to the characterization of accelerator magnet behavior, the primary focus of this research is the mechanics within the mesoscales in the system. In this regard, effects due to electromagnetism can be treated as lumped macroscale loads applied at the largest scale. However, for a complete understanding of the underlying physics, the electromagnetic equations relating to accelerator magnets are discussed in the following sections. For a more indepth examination, the reader is directed to works by Zohdi [89], Purcell [66], and Ida [39].

### 3.1.1 Current Density

Electric Current is the rate of transport of electric charge through a point or surface. The total current through a surface in the body $\Omega$ is

$$I = \int_A \mathbf{J} \cdot \mathbf{n} \mathrm{d}A, \tag{3.1}$$

where **J** is the current density, $A$ is the surface in which current is passing through, and **n** is the surface normal. This schematic is shown in figure 3.1.

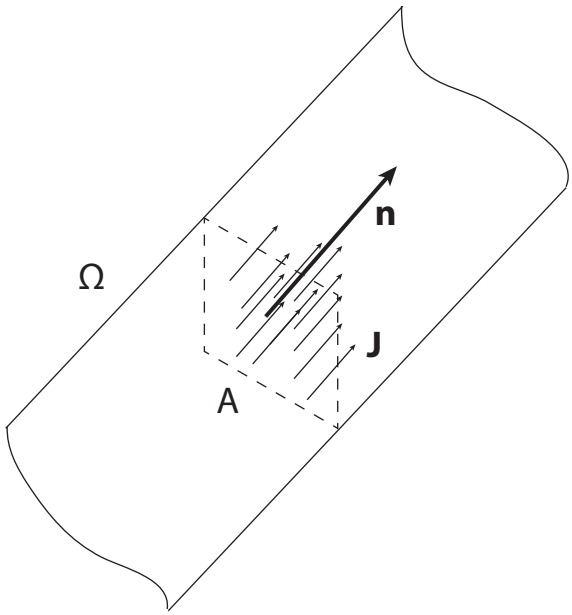


Figure 3.1: Current Through a Surface.

### 3.1.2 Maxwell's Equations

The fundamental definitions associated with electromagnetic occurences arise from Maxwell's equations. Namely: Gauss' Law, Gauss' Law of Magnetism, Maxwell-Faraday's Law, and Ampere's Law.

#### Gauss' Law

Gauss' Law is the first of Maxwell's equations, and dictates how the electric field behaves around electric charges. It is given in point form as

$$\nabla_x \cdot \mathbf{D} = \rho_f, \tag{3.2}$$

where $\nabla_x$ is the divergence of a tensor with respect to the current configuration, $D$ is the electric flux density and $\rho_f$ is the free charge density. Integrating over the volume and using the divergence theorem, we obtain the integral form as

$$\oint_{\partial\Omega} \mathbf{D} \cdot \mathrm{d}\mathbf{S} = Q_f, \tag{3.3}$$

where $\partial\Omega$ is the boundary of the body, $Q_f$ is the net free electric charge within the body's volume, and $\mathrm{d}\mathbf{S}$ is the differential vector element of surface area $S$, which is defined as $\mathrm{d}\mathbf{S} = \mathbf{n}\mathrm{d}A$.

### Gauss' Law of Magnetism

The magnetic flux through a surface is defined as

$$\Phi = \int_A \mathbf{B} \cdot \mathbf{n}\mathrm{d}A. \tag{3.4}$$

In an electric field, the electric flux originates at a positive charge and terminates on a negative charge. However, there are no magnetic charges analogous to electric charges (citation needed). Therefore, the entirity of magnetic flux entering a closed surface must also leave the closed surface. This is mathematically expressed by point form of Gauss' law of magnetism:

$$\nabla_x \cdot \mathbf{B} = 0. \tag{3.5}$$

Integrating over the volume and using the divergence theorem, we obtain the integral form as

$$\oint_{\partial\Omega} \mathbf{B} \cdot \mathrm{d}\mathbf{S} = 0. \tag{3.6}$$

### Maxwell-Faraday's Law

Maxwell-Faraday's Law describes how a time-varying magnetic field induces an electric field. In point form, it is given as

$$\nabla_x \times \mathbf{E} = -\frac{\partial \mathbf{B}}{\partial t}, \tag{3.7}$$

where $\nabla_x \times$ is the curl operator, E is the electric field intensity, and t is time. Using Stoke's theorem, we can obatin the integral form as

$$\oint_{\partial A} \mathbf{E} \cdot \mathrm{d}\mathbf{L} = -\frac{\mathrm{d}}{\mathrm{d}t} \int_A \mathbf{B} \cdot \mathrm{d}\mathbf{S}, \tag{3.8}$$

where $\partial A$ is the boundary of a surface and $\mathrm{d}\mathbf{L}$ is the differential vector element of the path length tangential to the curve.

**Ampere's Law**

Ampere's Law states that magnetic fields can be generated by electrical current as well as changing electric fields. The point form of this equation is given as

$$\nabla_x \times \mathbf{H} = \mathbf{J}_f + \frac{\partial \mathbf{D}}{\partial t}, \tag{3.9}$$

where $\mathbf{J}_f$ is the free current density. Integrating and using Stoke's theorem, the integral form is obtained as

$$\oint_{\partial A} \mathbf{H} \cdot \mathrm{d}\mathbf{L} = I_f + \int_A \frac{\partial \mathbf{D}}{\partial t} \cdot \mathrm{d}\mathbf{S}, \tag{3.10}$$

where $I_f$ is the net free electrical current passing through the surface $A$:

$$I_f = \int_A \mathbf{J_f} \cdot \mathbf{n} \mathrm{d}A. \tag{3.11}$$

## 3.2 Mechanics of Materials

In order to obtain the stress-strain configuration within the mesoscales of an accelerator magnet, balance laws must be satisfied. Namely, the balance of mass, balance of momentum, balance of angular momentum, and the balance of energy. Matter is treated as a continuous material, since the physical problem of interest occurs at sufficiently larger length and time scales than the characteristic scales. Therefore, a finite amount of matter within a body has physical properties that are independent over the size and time in whcih they are measured. For more information, the reader is directed to Gurtin [31], Chadwick [7], Malvern [51], Marsden [52], and Fung [23].

### 3.2.1 A Brief Review of Continuum Mechanics

Consider a body $\mathcal{B}$ and a configuration of the body $\mathcal{R}$, which is a subset of $\mathcal{E}^3$ occupied by $\mathcal{B}$ at time $t$. $\mathbf{x}$ is the location of a particle $\mathcal{P}$ at time $t$ relative to fixed origin $\mathcal{O}$. Similarly, a fixed configuration of the body at time $t_0$ can be used as a reference configuration $\mathcal{R}_0$.

A smooth motion, $\chi_t$ is used to map the reference configuration to the current configuration. Similarly, $\overline{\chi}_{t_0}$ maps the point $\mathcal{P}$ to reference location $\mathbf{X}$ and $\overline{\chi}_t$ maps the point $\mathcal{P}$ to the current location $\mathbf{x}$. This schematic can be visualized in figure 3.2.

The velocity and acceleration of points on the body can be determined by taking

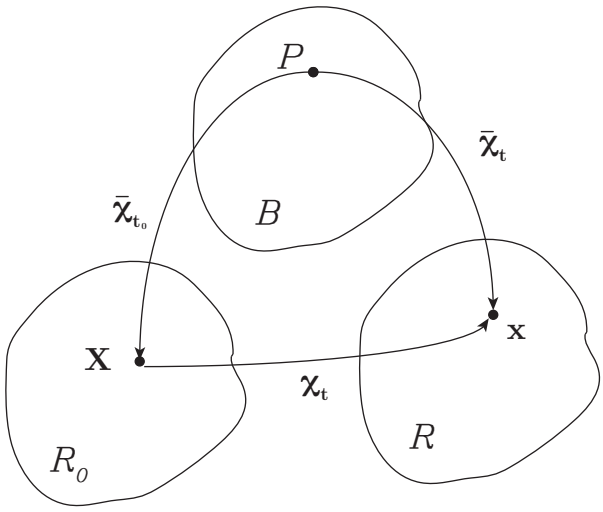


Figure 3.2: Diagram of body $\mathcal{B}$, it's reference configuration $\mathcal{R}_0$, and it's current configuration $\mathcal{R}$.

time derivatives of the motion $\chi_t$:

$$\mathbf{v} = \frac{\partial \chi_t(\mathbf{X}, t)}{\partial t}, \mathbf{a} = \frac{\partial \chi_t^2(\mathbf{X}, t)}{\partial t^2}. \tag{3.12}$$

Similarly, a deformation gradient is defined by taking a spacial derivative of the motion:

$$\mathbf{F} = \frac{\partial \chi_t(\mathbf{X}, t)}{\partial \mathbf{X}} = \frac{\partial(\mathbf{X} + \hat{\mathbf{u}}(\mathbf{X}, t))}{\partial \mathbf{X}} = \mathbf{I} + \frac{\partial \hat{\mathbf{u}}}{\partial \mathbf{X}} = \mathbf{I} + \mathbf{H}, \tag{3.13}$$

where $\mathbf{u}$ is the displacement vector defined as

$$\mathbf{u} = \hat{\mathbf{u}}(\mathbf{X}, t) = \tilde{\mathbf{u}}(\mathbf{x}, t), \tag{3.14}$$

$\mathbf{I}$ is the $3 \times 3$ identity tensor, and $\mathbf{H}$ is the relative displacement gradient tensor. The Jacobian, $J$ is defined to be the determinant of the deformation gradient, and maps an infinitessimal volume in the reference configuration to the current configuration as follows:

$$\mathrm{d}v = J\mathrm{d}V. \tag{3.15}$$

Strain is a measure of deformation representing the displacement between particles in the body at the current state relative to a reference length. The Lagrangian strain tensor can be defined as

$$\mathbf{E} = \frac{1}{2}\left(\mathbf{F}^T\mathbf{F} - \mathbf{I}\right). \tag{3.16}$$

### 3.2.2 Mass Balance

Consider a body $\mathcal{B}$ and a region within the body $\mathcal{S}$, shown in figure 3.3. The corresponding regions in the reference configuration and current configuration are $\mathcal{P}_0$ and $\mathcal{P}$, respectively. The balance of mass states that mass cannot change within the

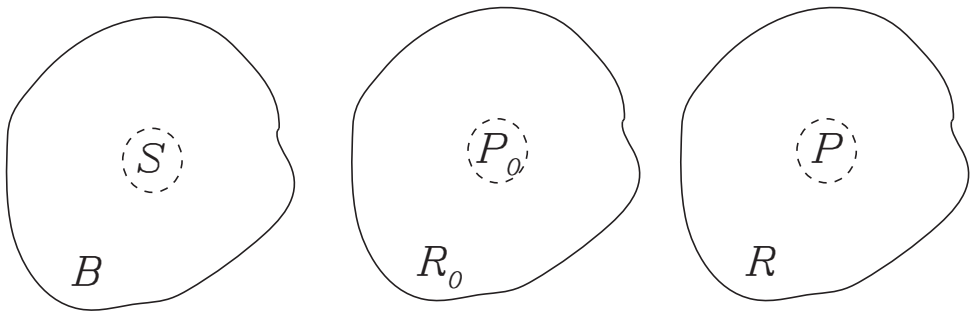


Figure 3.3: Diagram of body $\mathcal{B}$ .

subregion $\mathcal{S}$ over time. This can be written as

$$\int_{\mathcal{P}} \rho \mathrm{d}v = \int_{\mathcal{P}_0} \rho_0 \mathrm{d}V = \int_{\mathcal{P}_0} \rho J \mathrm{d}V. \tag{3.17}$$

where $\rho$ is the density of the material. Localizing, we obtain

$$\rho_0 = \rho J. \tag{3.18}$$

Using the Reynolds transport theorem on a scalar $f$,

$$\frac{\mathrm{d}}{\mathrm{d}t} \int_{\mathcal{P}(t)} f \mathrm{d}v = \int_{\mathcal{P}(t)} \left( \dot{f} + f \nabla_{\mathbf{x}} \cdot \mathbf{v} \right) \mathrm{d}v, \tag{3.19}$$

we can obtain an alternative definition of mass balance:

$$\dot{\rho} + \rho \nabla_{\mathbf{x}} \cdot \mathbf{v} = 0. \tag{3.20}$$

### 3.2.3 Alternative Representations of Maxwell's Equations

Current work with nonlinear electrodynamics of continua has been greatly influenced by Kovetz [45], who has presented postulates concerning the laws of motion, conservation of energy, and dissipation. The following derviation is detailed in work by Steigmann [73].

The principle of charge conservation within a material region $\mathcal{P}$ can be stated as

$$\int_{\mathcal{P}} \frac{\mathrm{d}q}{\mathrm{d}t} \mathrm{d}v + \int_{\partial\mathcal{P}} q\mathbf{v} \cdot \mathbf{n} \mathrm{d}a = \int_{\partial\mathcal{P}} \alpha \mathrm{d}a, \tag{3.21}$$

where $q(\mathbf{x}, t)$ is the charge per unit volume and $\alpha$ is the current flux per unit area. Application of Cauchy's theorem [31] gives

$$\alpha = -\mathcal{J} \cdot \mathbf{n}, \tag{3.22}$$

where $\mathcal{J}(\mathbf{x}, t)$ is the conduction current. For fields that are smooth, localization of the charge-conservation law yields

$$\frac{\mathrm{d}q}{\mathrm{d}t} + \nabla_{\mathbf{x}} \cdot \mathbf{j} = 0, \tag{3.23}$$

where $\mathbf{j} = q\mathbf{v} + \mathcal{J}$ is the net current.

Two of Maxwell's equations arise through the integration of the local charge-conservation law as a pair of vector potentials:

$$q = \nabla_{\mathbf{x}} \cdot \mathbf{d} \quad \text{and} \quad \mathbf{j} = \nabla_{\mathbf{x}} \times \mathbf{h} - \frac{\mathrm{d}\mathbf{d}}{\mathrm{d}t}, \tag{3.24}$$

where $\mathbf{d}(\mathbf{x}, t)$ is the electric displacement field and $\mathbf{h}(\mathbf{x}, t)$ is the magnetic field. The second pair of Maxwell's equations are given in local form by

$$\nabla_{\mathbf{x}} \cdot \mathbf{b} = 0 \quad \text{and} \quad \nabla_{\mathbf{x}} \times \mathbf{e} - \frac{\mathrm{d}\mathbf{b}}{\mathrm{d}t}, \tag{3.25}$$

where $\mathbf{e}(\mathbf{x}, t)$ is the electric field and $\mathbf{b}(\mathbf{x}, t)$ is the magnetic induction. These local forms are equivalent to their global counterparts whenever the fields are smooth.

### 3.2.4 Linear Momentum Balance

The linear momentum of the region $\mathcal{P}$ at time $t$, represented in figure 3.3, can be written as

$$\int_{\mathcal{P}} \rho\mathbf{v} \mathrm{d}v. \tag{3.26}$$

We admit three types of external forces on $\mathcal{P}$: body forces $\bar{\mathbf{b}}(\mathbf{x}, t)$ per unit mass, surface tractions $\bar{\mathbf{t}}(\mathbf{x}, t; \mathbf{n})$ per unit area on the boundary of $\mathcal{P}$, and the force on charged particles relative to an inertial frame of reference, known as the Lorentz force. The Lorentz force exerted on a material occupying a region $\mathcal{P}$ is

$$\mathbf{f}(\mathcal{P}, t) = \int_{\mathcal{P}} q\mathcal{E} \mathrm{d}v, \tag{3.27}$$

where $\mathcal{E} = \mathbf{e} + \mathbf{v} \times \mathbf{b}$. The following relation can then be derived[18]:

$$\mathbf{f}(\mathcal{P}, t) = \int_{\partial\mathcal{P}} \hat{\mathbf{T}}\mathbf{n}\mathrm{d}a - \varepsilon_0 \frac{\mathrm{d}}{\mathrm{d}t} \int_{\mathcal{P}} \mathbf{e} \times \mathbf{b}\mathrm{d}v, \tag{3.28}$$

where $\partial\mathcal{P}$ is the boundary of $\mathcal{P}$ and $\mathrm{d}a$ is the differential element of surface area and $\varepsilon_0$ is a positive constant such that $\mathbf{d} = \varepsilon_0\mathbf{e}$. In addition,

$$\hat{\mathbf{T}} = \mathbf{T}_M + \varepsilon_0 \mathbf{e} \times \mathbf{b} \otimes \mathbf{v}, \tag{3.29}$$

where $\mathbf{T}_M$ is the Maxwell stress.

The balance of linear momentum then follows as

$$\frac{\mathrm{d}}{\mathrm{d}t} \int_{\mathcal{P}} \rho\mathbf{v}\mathrm{d}v = \int_{\mathcal{P}} \rho\bar{\mathbf{b}}\mathrm{d}v + \int_{\partial\mathcal{P}} \bar{\mathbf{t}}\mathrm{d}a + \mathbf{f}(\mathcal{P}, t). \tag{3.30}$$

Noting Cauchy's theorem,

$$\bar{\mathbf{t}} = \bar{\mathbf{T}}\mathbf{n}, \tag{3.31}$$

the blance of linear momentum can be written as

$$\frac{\mathrm{d}}{\mathrm{d}t} \int_{\mathcal{P}} \rho\mathbf{g}\mathrm{d}v = \int_{\mathcal{P}} \rho\bar{\mathbf{b}}\mathrm{d}v + \int_{\partial\mathcal{P}} \mathbf{t}\mathrm{d}a, \tag{3.32}$$

where

$$\mathbf{g} = \mathbf{v} + \frac{\varepsilon_0}{\rho}\mathbf{e} \times \mathbf{b} \quad \text{and} \quad \mathbf{t} = \bar{\mathbf{t}} + \hat{\mathbf{T}}\mathbf{n}. \tag{3.33}$$

Through use of the divergence theorem, we can obtain the local form of linear momentum balance as follows:

$$\nabla_{\mathbf{x}} \cdot \mathbf{T} + \rho\bar{\mathbf{b}} = \rho\dot{\mathbf{g}}. \tag{3.34}$$

In the case where electromagnetic effects can be neglected, the local balance of linear momentum can be reduced to

$$\nabla_{\mathbf{x}} \cdot \bar{\mathbf{T}} + \rho\bar{\mathbf{b}} = \rho\mathbf{a}. \tag{3.35}$$

In referential form, this can be written as

$$\nabla_{\mathbf{X}} \cdot \mathbf{P} + \rho_0\mathbf{b} = \rho_0\mathbf{a}, \tag{3.36}$$

where $\mathbf{P}$ is the first Piola-Kirchhoff stress:

$$\mathbf{P} = J\bar{\mathbf{T}}\mathbf{F}^{-T}. \tag{3.37}$$

### 3.2.5 Angular Momentum Balance

Angular momentum balance simply results in symmetry of the Cauchy stress tensor:

$$\bar{\mathbf{T}} = \bar{\mathbf{T}}^T. \tag{3.38}$$

In referential form, this is written as

$$\mathbf{P}\mathbf{F}^T = \mathbf{F}\mathbf{P}^T. \tag{3.39}$$

Alternatively, the angular momentum balance can be written in the global form,

$$\frac{\mathrm{d}}{\mathrm{d}t}\int_{\mathcal{P}} (\mathbf{x}-\mathbf{x}_0)\times\rho\mathbf{g}\mathrm{d}v = \int_{\partial\mathcal{P}} (\mathbf{x}-\mathbf{x}_0)\times\mathbf{T}\mathbf{n}\mathrm{d}a + \int_{\mathcal{P}} (\mathbf{x}-\mathbf{x}_0)\times\bar{\mathbf{b}}\mathrm{d}v, \tag{3.40}$$

where $\mathbf{x}_0$ is the location of a reference point $O$.

### 3.2.6 Energy Balance

Admitting a heat supply per unit mass, $r(\mathbf{x},t)$, heat flux per unit area, $h(\mathbf{x},t;\mathbf{n})$, and internal energy per unit mass, $\varepsilon(\mathbf{x},t)$, we can formulate the local statement of energy balance as follows[73]:

$$\rho\dot{\varepsilon} = \rho\bar{\mathbf{b}}\cdot\mathbf{v} + \nabla\cdot\left(\mathbf{T}^T\mathbf{v}\right) + \rho r - \nabla_{\mathbf{x}}\cdot\left(\mathbf{q}+\mathcal{E}\times\mathcal{H}_f\right), \tag{3.41}$$

where $\mathbf{q}$ is the heat flux vector defined from the relation

$$h = \mathbf{q}\cdot\mathbf{n}, \tag{3.42}$$

and

$$\mathcal{H}_f = (\mathbf{h}-\mathbf{v}\times\mathbf{d}) - (\mathbf{m}+\mathbf{v}\times\mathbf{p}), \tag{3.43}$$

where $\mathbf{p}(\mathbf{x},t)$ and $\mathbf{m}(\mathbf{x},t)$ are the polarization and magnetic fields, respectively.

### 3.2.7 Constitutive Equations

A consitutive relation is the relation between two physical quantities that is specific to a material and approximates the response of that material to external stimuli. In the case of solid mechanics, the constitutive relation relates applied stresses or forces to strains or deformations, which before accounting for possible restrictions or reductions can be written as

$$\mathbf{T} = \tilde{\mathbf{T}}\left(\mathbf{x},\mathbf{v},\mathbf{F},\dot{\mathbf{F}},...,\nabla_{\mathbf{X}}\mathbf{F},...,\rho,\dot{\rho}...\right). \tag{3.44}$$

Since electromagnetic effects are not considered within the test cases considered in Chapter 6, these terms are left out of the following constitutive equations.

### Linear Elasticity

The fundamental linearizing assumptions of linear elasticity are:

1. Infinitesimal strains, i.e. small deformations
2. Linear relationships between the components of stress and strain

The first assumption reduces equation 3.16 to the infinitessimal strain tensor

$$\boldsymbol{\varepsilon} = \frac{1}{2}\left(\mathbf{H} + \mathbf{H}^T\right). \tag{3.45}$$

The second assumption leads to the following relationship between the stress and strain tensors:

$$\boldsymbol{\sigma} = \mathbf{C} \cdot \boldsymbol{\varepsilon}, \tag{3.46}$$

where $\boldsymbol{\sigma}$ is the infinitessimal stress tensor and $\mathbf{C}$ is the fourth-order elasticity tensor containing constants. In general, this fourth-order elasticity tensor possesses 81 material constants. However, due to 3.38 and the symmetry of $\boldsymbol{\varepsilon}$ apparent in 3.45, it follows that

$$C_{ijkl} = C_{jikl} = C_{ijlk} = C_{jilk}, \tag{3.47}$$

implying that only 36 of the components are independent. Equation 3.46 can then be reorganized and written as

$$\begin{bmatrix} \sigma_{11} \\ \sigma_{22} \\ \sigma_{33} \\ \sigma_{12} \\ \sigma_{23} \\ \sigma_{31} \end{bmatrix} = \begin{bmatrix} C_{11} & C_{12} & C_{13} & C_{14} & C_{15} & C_{16} \\ C_{21} & C_{22} & C_{23} & C_{24} & C_{25} & C_{26} \\ C_{31} & C_{32} & C_{33} & C_{34} & C_{35} & C_{36} \\ C_{41} & C_{42} & C_{43} & C_{44} & C_{45} & C_{46} \\ C_{51} & C_{52} & C_{53} & C_{54} & C_{55} & C_{56} \\ C_{61} & C_{62} & C_{63} & C_{64} & C_{65} & C_{66} \end{bmatrix} \begin{bmatrix} \varepsilon_{11} \\ \varepsilon_{22} \\ \varepsilon_{33} \\ 2\varepsilon_{12} \\ 2\varepsilon_{23} \\ 2\varepsilon_{31} \end{bmatrix}. \tag{3.48}$$

Two types of linear elastic materials are used in the analysis of accelerator magnets: isotropic and orthotropic materials. In the case of isotropy, the material exhibits an idential response regardless of orientation. The elasticity tensor is reduced to two independent components and can be written as

$$\begin{bmatrix} \lambda + 2\mu & \lambda & \lambda & 0 & 0 & 0 \\ \lambda & \lambda + 2\mu & \lambda & 0 & 0 & 0 \\ \lambda & \lambda & \lambda + 2\mu & 0 & 0 & 0 \\ 0 & 0 & 0 & \mu & 0 & 0 \\ 0 & 0 & 0 & 0 & \mu & 0 \\ 0 & 0 & 0 & 0 & 0 & \mu \end{bmatrix}, \tag{3.49}$$

where $\lambda$ and $\mu$ are Lamé parameters. The orthotropic elasticity tensor can be written as

$$\begin{bmatrix} C_{11} & C_{12} & C_{13} & 0 & 0 & 0 \\ C_{12} & C_{22} & C_{23} & 0 & 0 & 0 \\ C_{13} & C_{23} & C_{33} & 0 & 0 & 0 \\ 0 & 0 & 0 & C_{44} & 0 & 0 \\ 0 & 0 & 0 & 0 & C_{55} & 0 \\ 0 & 0 & 0 & 0 & 0 & C_{66} \end{bmatrix}, \tag{3.50}$$

with 9 independent material constants.

### Linear Thermoelasticity

With the inclusion of temperature dependence, the body develops stresses due to changes in temperature. Equation 3.46 becomes

$$\sigma_{ij} = -\beta_{ij}\left(\theta - \theta_0\right) + C_{ijkl}\varepsilon_{kl}, \tag{3.51}$$

where $\theta$ is the current material temperature, $\theta_0$ is the refrence material temperature, and $\boldsymbol{\beta}$ is a tensor of linear coefficients of thermal expansion. In the case of isotropy, this reduces to

$$\sigma_{ij} = \lambda\varepsilon_{kk}\delta_{ij} + 2\mu\varepsilon_{ij} - \beta\left(\theta - \theta_0\right)\delta_{ij}, \tag{3.52}$$

where $\delta_{ij}$ is the Kronecker delta.

### Plasticity

The primary limitation of elastic constitutive models is that they don't account for yielding of materials. Plasticity describes the process of a material undergoing irreversible changes in deformation in response to applied forces. For further information on classical rate-independent plasticity, refer to work by Green and Nagdi [25] [26] as well as Simo [70]. Consider a yield surface in six-dimensional stress space and strain space shown in figure 3.4, and given by the equation

$$f = \bar{f}\left(\mathbf{T}, \mathbf{q}\right) = \hat{f}\left(\mathbf{E}, \mathbf{q}\right) = 0, \tag{3.53}$$

where $\mathbf{q}$ represents internal variables. The material is taken to behave elastically within the yield surface, and plastically when the loading path reaches $f$. In the case of small deformations, this reduces to

$$f = \bar{f}\left(\boldsymbol{\sigma}, \mathbf{q}\right) = \hat{f}\left(\boldsymbol{\varepsilon}, \mathbf{q}\right) = 0, \tag{3.54}$$

In classical plasticity, one can assume an additive decomposition of the strain

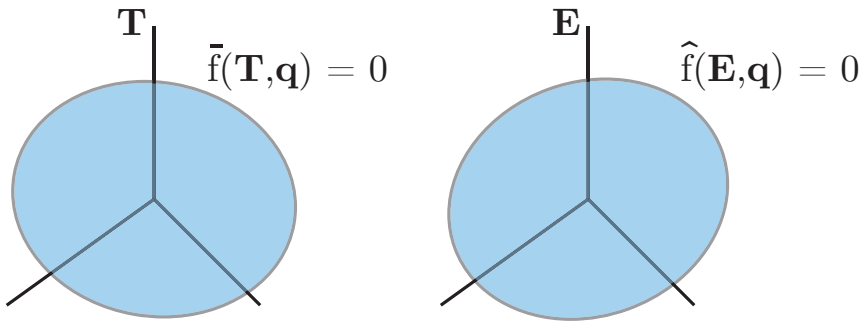


Figure 3.4: Yield Surfaces in Stress and Strain Space.

tensor:

$$\boldsymbol{\varepsilon} = \boldsymbol{\varepsilon}^e + \boldsymbol{\varepsilon}^p \tag{3.55}$$

where $\boldsymbol{\varepsilon}^e$ is the elastic part of the strain and $\boldsymbol{\varepsilon}^p$ is the plastic portion. The linear elastic response is then

$$\boldsymbol{\sigma} = -\boldsymbol{\beta}\left(\theta - \theta_0\right) + \mathbf{C} \cdot \left(\boldsymbol{\varepsilon} - \boldsymbol{\varepsilon}^p\right). \tag{3.56}$$

and is valid for $\bar{f}\left(\boldsymbol{\sigma}, \mathbf{q}\right) < 0$.

Now we introduce the idea of irreversibility of plastic flow through the inclusion of equations of evolution for $\boldsymbol{\varepsilon}^p$ and $\mathbf{q}$, called the flow rule and hardening law, respectively:

$$\begin{aligned} \dot{\boldsymbol{\varepsilon}}^p &= \gamma \mathbf{r}\left(\boldsymbol{\sigma}, \mathbf{q}\right) \\ \dot{\mathbf{q}} &= -\gamma \mathbf{h}\left(\boldsymbol{\sigma}, \mathbf{q}\right) \end{aligned} \tag{3.57}$$

where $\mathbf{r}$ and $\mathbf{h}$ are prescribed functions which define the direction of plastic flow and the type of hardening. The paramter $\gamma$ is called the consistency parameter, which is assumed to obey the following Kuhn-Tucker complementarity condistions [50]:

$$\begin{aligned} \gamma &\geq 0 \\ \bar{f}\left(\boldsymbol{\sigma}, \mathbf{q}\right) &\leq 0 \\ \gamma \bar{f}\left(\boldsymbol{\sigma}, \mathbf{q}\right) &= 0 \end{aligned} \tag{3.58}$$

as well as the consistency requirement

$$\gamma \dot{\bar{f}}\left(\boldsymbol{\sigma}, \mathbf{q}\right) = 0. \tag{3.59}$$

A common plasticity model is $J_2$ flow theory with isotropic and kinematic hardening, which is a typical model characterizing metal plasticity. In it

$$\mathbf{q} := \left\{\alpha, \bar{\boldsymbol{\beta}}\right\}, \tag{3.60}$$

where $\bar{\boldsymbol{\beta}}$ is the back-stress, denoting the center of the yield surface, and $\alpha$ is the equivalent plastic strain that defines isotropic hardening of the von Mises yield surface. We denote $\mathbf{s}$ and $\mathbf{e}$ to be the deviatoric stress and strain tensors:

$$\mathbf{s} = \boldsymbol{\sigma} - \tfrac{1}{3}\left(\mathrm{tr}\boldsymbol{\sigma}\right)\mathbf{I}, \quad \mathbf{e} = \boldsymbol{\varepsilon} - \tfrac{1}{3}\left(\mathrm{tr}\boldsymbol{\varepsilon}\right)\mathbf{I}. \tag{3.61}$$

For rate-independent plasticity with von-Mises pressure insensitive yield conditions, we have the following yield condition, flow rule, and hardening law:

$$\begin{gathered} \boldsymbol{\eta} := \mathbf{s} - \bar{\boldsymbol{\beta}}, \mathrm{tr}\bar{\boldsymbol{\beta}} = 0, \\ f\left(\boldsymbol{\sigma}, \mathbf{q}\right) = \|\boldsymbol{\eta}\| - \sqrt{\tfrac{2}{3}} K\left(\alpha\right), \\ \dot{\boldsymbol{\varepsilon}}^p = \gamma \tfrac{\boldsymbol{\eta}}{\|\boldsymbol{\eta}\|}, \\ \dot{\bar{\boldsymbol{\beta}}} = \gamma \tfrac{2}{3} H'\left(\alpha\right) \tfrac{\boldsymbol{\eta}}{\|\boldsymbol{\eta}\|}, \\ \dot{\alpha} = \gamma \sqrt{\tfrac{2}{3}}, \end{gathered} \tag{3.62}$$

where the functions $K'\left(\alpha\right)$ and $H'\left(\alpha\right)$ are the isotropic and kinematic hardening moduli and $\gamma = \|\dot{\boldsymbol{\varepsilon}}^p\|$. The following form of kinematic and isotropic hardening laws are widely used in computational implementations [37]:

$$\begin{aligned} H'\left(\alpha\right) &= \left(1 - \bar{\theta}\right)\bar{H}, \\ K\left(\alpha\right) &= \sigma_y + \bar{\theta}\bar{H}\alpha, \quad \bar{\theta} \in \left[0, 1\right], \end{aligned} \tag{3.63}$$

where $\bar{H}$ is a constant and $\sigma_y$ is the yield stress.

The plastic consistency paramter in the general case takes the explicit form

$$\gamma = \tfrac{\langle \mathbf{n} : \dot{\boldsymbol{\varepsilon}} \rangle}{1 + \frac{H' + K'}{3\mu}}, \quad \mathbf{n} := \tfrac{\boldsymbol{\eta}}{\|\boldsymbol{\eta}\|}. \tag{3.64}$$

For plastic loading, when $\gamma > 0$, the elastoplastic tangulent modulus is

$$\mathbf{C}^{ep} = \kappa \mathbf{1} \otimes \mathbf{1} + 2\mu \left[ \mathbf{I} - \frac{1}{3}\mathbf{1} \otimes \mathbf{1} - \frac{\mathbf{n} \otimes \mathbf{n}}{1 + \frac{H' + K'}{3\mu}} \right], \tag{3.65}$$

where $\kappa$ is the bulk modulus, $\mathbf{1} = \delta_{ij}\mathbf{e}_i \otimes \mathbf{e}_j$, $\mathbf{I} = \frac{1}{2}\left[\delta_{ik}\delta_{jl} + \delta_{il}\delta_{jk}\right]\mathbf{e}_i \otimes \mathbf{e}_j \otimes \mathbf{e}_k \otimes \mathbf{e}_l$, and $\otimes$ is the outer product operator.

### 3.2.8 Material Properties

The primary materials considered within a model are $Nb_3Sn$, Copper, and Bronze. The following material responses have been compiled by Mitchell [55] and are plotted in figures 3.5 through 3.8. Within the plastic range of materials, a power law expression is used. To enforce continuity of stress-strain curves for elasto-plastic materials,

the power law is modified as

$$\varepsilon = A\sigma^n + \sigma/E \tag{3.66}$$

with

$$n = \ln\left(\varepsilon_u - \frac{\sigma_u}{E\varepsilon_y} - \frac{\sigma_y}{E}\right)/\ln\left(\frac{\sigma_u}{\sigma_y}\right), \tag{3.67}$$

and

$$A = \varepsilon_u - \frac{\sigma_u}{E\sigma_u^n}, \tag{3.68}$$

where $\sigma_u$, $\varepsilon_u$ is the ultimate tensile strain, and $\varepsilon_y - \sigma_y/E$ is the 0.002 offset strain.

$Nb_3Sn$

The material is assumed to not yield in compression, and due to it's brittle behavior assumed to behave elastically. Refences [15] [21] [22] report modulus as a function of temperature, with the drop in modulous being dependent on the alloying materials. The modulus is given as

$$E = \begin{cases} 100 \text{ GPa} & T < 35 \text{ K} \\ 100 + 35\,(T - 35)\,/65 \text{ GPa} & 35 < T < 100 \text{ K} \\ 135 \text{ GPa} & T > 100 \text{ K} \end{cases}. \tag{3.69}$$

Poissons ratio was taken to be 0.3, due to the lack of data.

The thermal expansion properties for $Nb_3Sn$ are given by [88] as

$$\Delta L/L = -0.187 + 5.490 \times 10^{-4}T + 3.296 \times 10^{-7}T^2 - 8.261 \times 10^{-11}T^3 \tag{3.70}$$

for temperatures from 0 to 1300 K, where $\Delta L$ is the change relative to the length at 293 K.

### Copper

The mechanical properties for copper comes from [60] and are

$$\begin{gathered} \sigma_u = 315 - 0.5625T + 2.925 \times 10^{-4}T^2 \text{ MPa}, \\ \sigma_y = 86.8 - 0.154T + 0.805 \times 10^{-4}T^2 \text{ MPa}, \\ E = 137 - 1.270 \times 10^{-4}T^2 + 8.00 \times 10^{-8}T^3 \text{ GPa}, \\ \varepsilon_u = 58.4 - 0.0553T - 15\,(1000 - T)\,/1000 + 1.0 \times 10^{-5}T^2 \text{ \%}. \end{gathered} \tag{3.71}$$

The thermal expansion properties for copper are given by [88] as

$$\begin{gathered} \Delta L/L = -0.33549 + 0.44671 \times 10^{-3}T + 2.9777 \times 10^{-6}T^2 \\ -2.6684 \times 10^{-9}T^3 + 9.4064 \times 10^{-13}T^4 \end{gathered} \tag{3.72}$$

and are valid from 1 K to 1300 K.

### Bronze

From reference [88], the differences between the expansion of pure copper and bronze in the range of $300 - 775$ K are small and the thermal expansion of copper can be used as a replacement. Due to uncertain Tin compositions within the accelerator magnets, the material properties for copper are used in place of bronze as well.

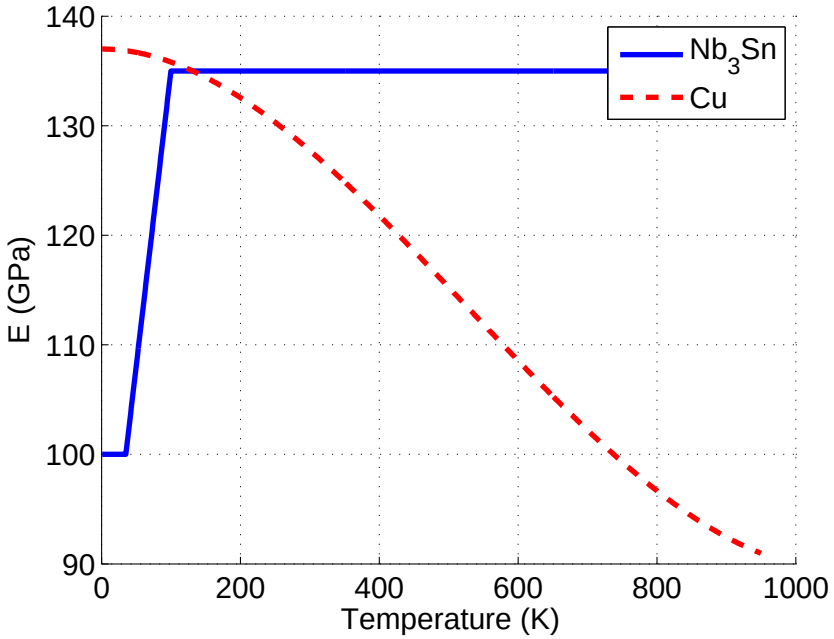


Figure 3.5: Young's Modulus for $Nb_3Sn$ and Copper.

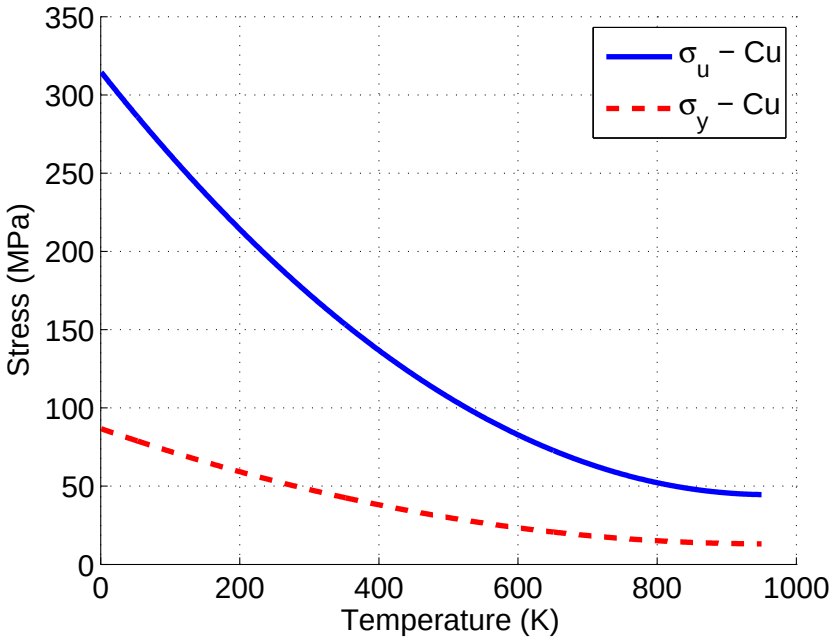


Figure 3.6: Ultimate Stress and Yield Stress for Copper.

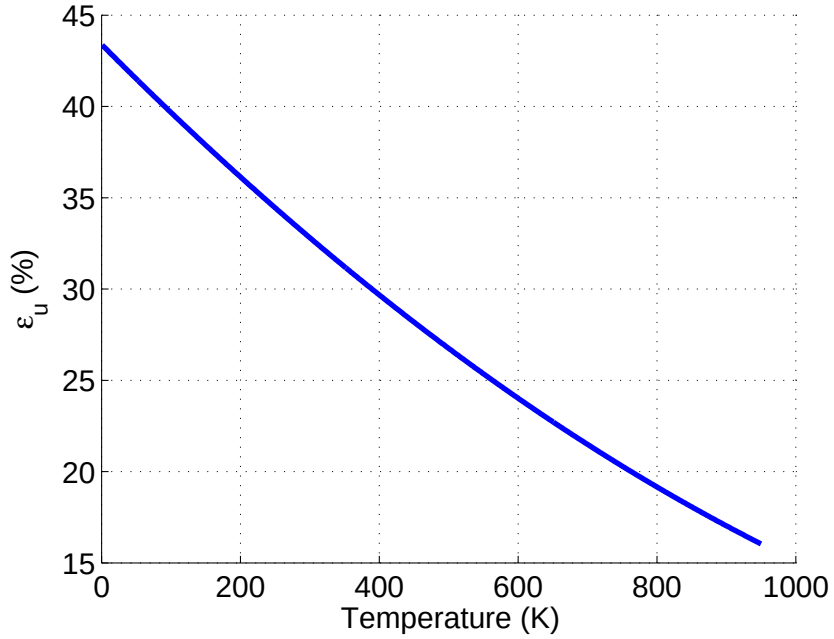


Figure 3.7: Ultimate Tensile Strain for Copper.

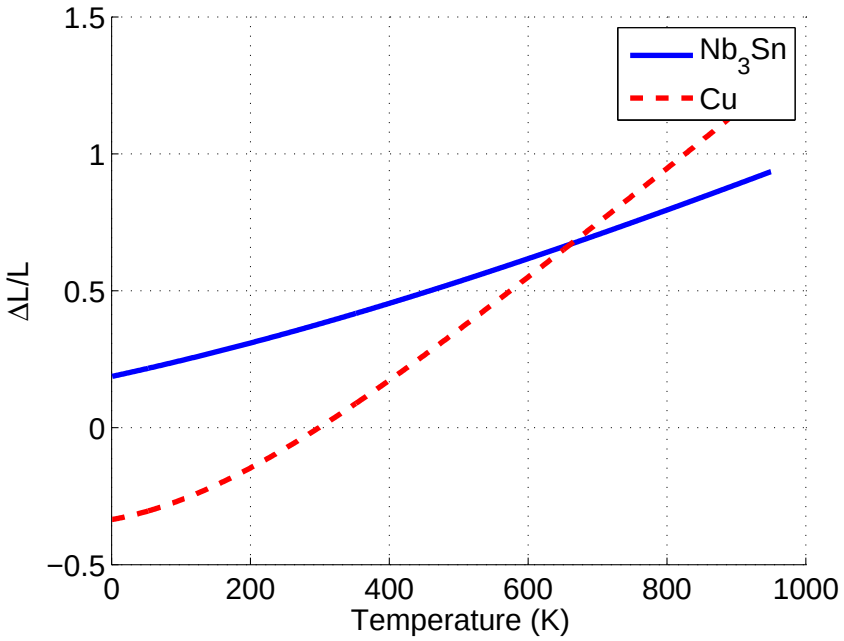


Figure 3.8: Thermal Expansion for $Nb_3Sn$ and Copper.

# Chapter 4

# Numerical Methods and Algorithms

In this section, the methods necessary to numerically implement previous governing equations are discussed with the exception of multiscale modeling, which will be examined in closer detail in the following chapter.

Due to the complex geometry, loading conditions, and material behavior that arises within a superconducting accelerator magnet, it would be infeasible to attempt a closed form solution to the governing equations. Instead, approximate numerical methods are needed, with the finite element method being implemented in the present work. A Lagrangian mesh, where nodal points are fixed to material points on the body, is used for the discretization of bodies. This causes the mass balance equation, 3.18, to be satisfied implicitly.

## 4.1 Radial Return Mapping Algorithm

To address the plastic material behavior present, a procedure for implementing the formulation in the previous chapter, called return mapping [70] [71], is employed. The algorithm, developed by Simo and Taylor, which addresses associative $J_2$ flow rules with general nonlinear kinematic and isotropic hardening rules is given in the following list.

*Box 1: Radial return algorithm*:

1. Compute trial elastic stress.

$$\mathbf{e}_{n+1} = \boldsymbol{\varepsilon}_{n+1} - \frac{1}{3}\mathrm{tr}\boldsymbol{\varepsilon}_{n+1}\mathbf{1}$$
$$\mathbf{s}_{n+1}^{\mathrm{trial}} = 2\mu\left(\mathbf{e}_{n+1} - \mathbf{e}_n^p\right)$$
$$\boldsymbol{\xi}_{n+1}^{\mathrm{trial}} = \mathbf{s}_{n+1}^{\mathrm{trial}} - \bar{\boldsymbol{\beta}}_n$$

2. Check yield condition:

$$f_{n+1}^{\mathrm{trial}} := \left\|\boldsymbol{\xi}_{n+1}^{\mathrm{trial}}\right\| - \sqrt{\frac{2}{3}}K\left(\alpha_n\right)$$
IF $f_{n+1}^{\mathrm{trial}} \leq 0$ THEN :
SET $\left(\cdot\right)_{n+1} = \left(\cdot\right)_{n+1}^{\mathrm{trial}}$ AND EXIT
ENDIF

3. Compute $\mathbf{n}_{n+1}$ and find $\Delta\gamma$ from Box 2. Set:

$$\mathbf{n}_{n+1} := \frac{\boldsymbol{\xi}_{n+1}^{\mathrm{trial}}}{\left\|\boldsymbol{\xi}_{n+1}^{\mathrm{trial}}\right\|},$$
$$\alpha_{n+1} := \alpha_n + \sqrt{\frac{2}{3}}\Delta\gamma$$

4. Update back stress, plastic strain and stress

$$\bar{\boldsymbol{\beta}}_{n+1} = \bar{\boldsymbol{\beta}}_n + \sqrt{\frac{2}{3}}\left(H\left(\alpha_{n+1}\right) - H\left(\alpha_n\right)\right)\mathbf{n}_{n+1}$$
$$\mathbf{e}_{n+1}^p = \mathbf{e}_n^p + \Delta\gamma\mathbf{n}_{n+1}]$$
$$\boldsymbol{\sigma}_{n+1} = \kappa\mathrm{tr}\boldsymbol{\varepsilon}_{n+1}\mathbf{1} + \mathbf{s}_{n+1}^{\mathrm{trial}} - 2\mu\Delta\gamma\mathbf{n}_{n+1}$$

5. Compute consistent elastoplastic tangent moduli

$$\mathbf{C}_{n+1} = \kappa\mathbf{1}\otimes\mathbf{1} + 2\mu\theta_{n+1}\left[\mathbf{I} - \frac{1}{3}\mathbf{1}\otimes\mathbf{1}\right] - 2\mu\bar{\theta}_{n+1}\mathbf{n}_{n+1}$$
$$\theta_{n+1} := 1 - \frac{2\mu\Delta\gamma}{\left\|\boldsymbol{\xi}_{n+1}^{\mathrm{trial}}\right\|}$$
$$\bar{\theta}_{n+1} := \frac{1}{1 + \frac{\left[K'+H'\right]_{n+1}}{3\mu}} - \left(1 - \theta_{n+1}\right)$$

*Box 2: Consistency condition*:

1. Initialize.

$$\Delta\gamma^{(0)} = 0$$

$$\alpha_{n+1}^{(0)} = \alpha_n$$

2. Iterate.

DO UNTIL : $\left|g\left(\Delta\gamma^{(k)}\right)\right| < \text{TOL}$,

$k \leftarrow k+1$

(a) Compute iterate $\Delta\gamma^{(k+1)}$:

$$g\left(\Delta\gamma^{(k)}\right) := -\sqrt{\frac{2}{3}}K\left(\alpha_{n+1}^{(k)}\right) + \left\|\boldsymbol{\xi}_{n+1}^{\text{trial}}\right\| - \left\{2\mu\Delta\gamma^{(k)} + \sqrt{\frac{2}{3}}\left[H\left(\alpha_{n+1}^{(k)}\right) - H\left(\alpha_n\right)\right]\right\}$$

$$Dg\left(\Delta\gamma^{(k)}\right) := -2\mu\left\{1 + \frac{H'\left[\alpha_{n+1}^{(k)}\right] + K'\left[\alpha_{n+1}^{(k)}\right]}{3\mu}\right\}$$

$$\Delta\gamma^{(k+1)} = \Delta\gamma^{(k)} - \frac{g\left[\Delta\gamma^{(k)}\right]}{Dg\left[\Delta\gamma^{(k)}\right]}$$

(b) Update equivalent plastic strain.

$$\alpha_{n+1}^{(k+1)} = \alpha_n + \sqrt{\tfrac{2}{3}}\Delta\gamma^{(k+1)}$$

## 4.2 Finite Element Method

In this section we examine the finite element formulation of boundary-value problems. For a more in depth description, see Hughes [38], Oden [62], and Zienkiewicz [61]. Consider the infinitessimal elastoplastic boundary-value problem [30] [72] [76], where a body $\boldsymbol{\Omega}$, shown in figure 4.1, with boundary $\boldsymbol{\Gamma}$ is subjected to body forces $\mathbf{f}$, prescribed boundary displacements $q_i$ on $\boldsymbol{\Gamma}_{q_i}$, and prescribed boundary tractions $h_i$ on $\boldsymbol{\Gamma}_{h_i}$. A formal statement of the strong form of the boundary-value problem is

$$\begin{aligned} \sigma_{ij,j} + f_i = 0 \quad & \text{on } \boldsymbol{\Omega} \\ u_i = q_i \quad & \text{on } \boldsymbol{\Gamma}_{q_i} \\ \sigma_{ij} n_j = h_i \quad & \text{on } \boldsymbol{\Gamma}_{h_i} \end{aligned} \tag{4.1}$$

where $\mathbf{u}$ is the displacement of a material point.

Let $\mathcal{S}_i$ denote the trial solution space and $\mathcal{V}_i$ the variation space. Each member $u_i \in \mathcal{S}_i$ satisfies $u_i = q_i$ on $\boldsymbol{\Gamma}_{q_i}$, whereas each trial function $w_i \in \mathcal{V}_i$ satisfies $w_i = 0$ on $\boldsymbol{\Gamma}_{q_i}$. The weak form in three-dimensional space can be written as follows: Given $\mathbf{f}$, $\mathbf{q}$,

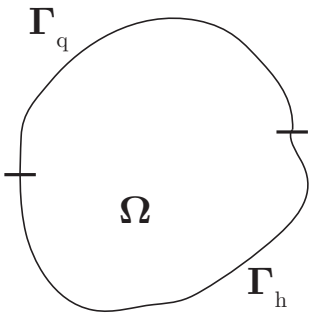


Figure 4.1: Body $\mathbf{\Omega}$.

and $\mathbf{h}$, find $\mathbf{u} \in \boldsymbol{\mathcal{S}}$ such that for all $\mathbf{w} \in \boldsymbol{\mathcal{V}}$

$$a(\mathbf{w}, \mathbf{u}) = (\mathbf{w}, \mathbf{f}) + (\mathbf{w}, \mathbf{h})_{\mathbf{\Gamma}}, \tag{4.2}$$

where

$$\begin{gathered} a(\mathbf{w}, \mathbf{u}) = \int_{\mathbf{\Omega}} w_{(i,j)} \sigma_{ij} \mathrm{d}\mathbf{\Omega} \\ (\mathbf{w}, \mathbf{f}) = \int_{\mathbf{\Omega}} w_i f_i \mathrm{d}\mathbf{\Omega} \\ (\mathbf{w}, \mathbf{h})_{\mathbf{\Gamma}} = \sum_{i=1}^{3} \left( \int_{\mathbf{\Gamma}_{h_i}} w_i h_i \mathrm{d}\mathbf{\Gamma} \right) \end{gathered} \tag{4.3}$$

### 4.2.1 Galerkin Formulation

We first discretize the body $\mathbf{\Omega}$ into finite elements, shown in figure 4.2. Let $\boldsymbol{\mathcal{S}}^h$ and $\boldsymbol{\mathcal{V}}^h$ be finite-dimensional approximations to $\boldsymbol{\mathcal{S}}$ and $\boldsymbol{\mathcal{V}}$, respectively. Assume members $\mathbf{w} \in \boldsymbol{\mathcal{V}}$ result in approximate satisfaction of the boundary condition $w_i = 0$ on $\mathbf{\Gamma}_{q_i}$.

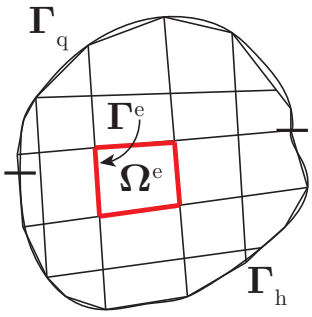


Figure 4.2: Body $\mathbf{\Omega}$ Discretized Into Elements $\mathbf{\Omega}^e$.

The Galerkin formulation [38] [70] of the elastoplastic problem is as follows: Given

$\mathbf{f}$, $\mathbf{q}$, and $\mathbf{h}$, find $\mathbf{u}^h \in \boldsymbol{\mathcal{S}}^h$ such that for all $\mathbf{w}^h \in \boldsymbol{\mathcal{V}}^h$

$$a\left(\mathbf{w}^h, \mathbf{u}^h\right) = \left(\mathbf{w}^h, \mathbf{f}\right) + \left(\mathbf{w}^{\mathbf{h}}, \mathbf{h}\right)_{\boldsymbol{\Gamma}}. \tag{4.4}$$

Define

$$\mathbf{f}_e^{\text{int}}\left(\boldsymbol{\sigma}^h\right) := \int_{\boldsymbol{\Omega}^e} \mathbf{B}_e^T \boldsymbol{\sigma}^h \mathrm{d}\boldsymbol{\Omega}, \tag{4.5}$$

and

$$\mathbf{f}_e^{\text{ext}} := -\int_{\boldsymbol{\Omega}^e} \mathbf{B}_e^T \bar{\boldsymbol{\sigma}}^h \mathrm{d}\boldsymbol{\Omega}, \tag{4.6}$$

where $\bar{\boldsymbol{\sigma}}^h$ are applied stresses and $\mathbf{B}_e$ for a local node takes the form

$$\mathbf{B}_a = \begin{bmatrix} N_{a,1} & 0 & 0 \\ 0 & N_{a,2} & 0 \\ 0 & 0 & N_{a,3} \\ 0 & N_{a,3} & N_{a,2} \\ N_{a,3} & 0 & N_{a,1} \\ N_{a,2} & N_{a,1} & 0 \end{bmatrix}. \tag{4.7}$$

Neglecting body forces and using the divergence thereom, one arrives at the discrete system of nonlinear differential equations:

$$\mathbf{F}^{\text{int}}\left(\boldsymbol{\sigma}^h\right) - \mathbf{F}^{\text{ext}} = \mathbf{0}, \tag{4.8}$$

where

$$\begin{aligned} \mathbf{F}^{\text{int}}\left(\boldsymbol{\sigma}^h\right) &= \overset{n_{el}}{\underset{e=1}{\mathbf{A}}} \mathbf{f}_e^{\text{int}}\left(\boldsymbol{\sigma}^h\right), \\ \mathbf{F}^{\text{ext}} &= \overset{n_{el}}{\underset{e=1}{\mathbf{A}}} \mathbf{f}_e^{\text{ext}}, \end{aligned} \tag{4.9}$$

where $\overset{n_{el}}{\underset{e=1}{\mathbf{A}}}$ is the assembly operator and $n_{el}$ is the number of elements.

### 4.2.2 Incremental Solution Procedure

The associated displacement field at a given load increment is $u_n^h$. Consider an incrememntal load $\Delta\bar{\boldsymbol{\sigma}}_n$ so that

$$\bar{\boldsymbol{\sigma}}_{n+1} = \bar{\boldsymbol{\sigma}}_n + \Delta\bar{\boldsymbol{\sigma}}_n \tag{4.10}$$

is the loading at $n+1$, which defines the discrete external load vector $\mathbf{F}_{n+1}^{\text{ext}}$. The problem can be defined as follows:

*Box 3: Incremental solution procedure*: Find $\Delta\mathbf{u}_n^h \in \boldsymbol{\mathcal{S}}^h$, the updated nodal displacement field $\mathbf{u}_{n+1}^h = \mathbf{u}_n^h + \Delta\mathbf{u}_{n+1}^h$, the updated internal variables $\left\{\boldsymbol{\varepsilon}_{n+1}^p, \alpha_{n+1}, q_{n+1}\right\}$, and the stress field $\boldsymbol{\sigma}_{n+1}^h$ such that

1. $\mathbf{F}^{\text{int}}\left(\boldsymbol{\sigma}^h\right) - \mathbf{F}^{\text{ext}} = \mathbf{0}$ and
2. The discrete constitutive equations in boxes 1 and 2 hold.

1. Let
$$\mathbf{u}_{n+1}^{(k)} := \mathbf{u}_n + \Delta\mathbf{u}_{n+1}^{(k)} \tag{4.11}$$
be the total nodal displacement at the $k$th iteration. The strain field is computed as
$$\boldsymbol{\varepsilon}_{n+1}^k|_{\boldsymbol{\Omega}^e} = \mathbf{B}_e\mathbf{u}_e|_{n+1}^{(k)}. \tag{4.12}$$

2. Given the strain field, compute the stress $\boldsymbol{\sigma}_{n+1}^{(k)}$ at each quadrature point using box 1 and 2.

3. Evaluate internal force fector $\mathbf{f}_e^{\text{int}}\left(\boldsymbol{\sigma}_{n+1}^h\right)$ and assemble as in equation 4.9.

4. Check convergence: if 4.8 is satisfied then exit; otherwise continue.

5. Determine $\Delta\mathbf{u}_{n+1}^{(k)}$, set $k \leftarrow k+1$ and go back to the first step.

The determination of $\Delta\mathbf{u}_{n+1}^{(k)}$ is performed using the following formula, which is equivalent to the classical Newtonian scheme:

$$\Delta\mathbf{u}_{n+1}^{(k+1)} = -\left[\mathbf{K}_{n+1}^{(k)}\right]^{-1}\left[\mathbf{F}^{\text{int}}\left(\boldsymbol{\sigma}_{n+1}^{(k)}\right) - \mathbf{F}_{n+1}^{\text{ext}}\right], \tag{4.13}$$

where

$$\mathbf{K}_{n+1}^{(k)} = \mathop{\mathsf{A}}_{e=1}^{n_{el}}\mathbf{k}_e|_{n+1}^{(k)}, \quad \mathbf{k}_e|_{n+1}^{(k)} = \int_{\boldsymbol{\Omega}^e}\mathbf{B}_e^T\left[\frac{\partial\boldsymbol{\sigma}_{n+1}^{(k)}}{\partial\boldsymbol{\varepsilon}_{n+1}^{(k)}}\right]\mathbf{B}_e\mathrm{d}\boldsymbol{\Omega}. \tag{4.14}$$

We can then note that

$$\frac{\partial\boldsymbol{\sigma}_{n+1}^{(k)}}{\partial\boldsymbol{\varepsilon}_{n+1}^{(k)}} = \mathbf{C}_{n+1}^{(k)}, \tag{4.15}$$

as given in box 1.

### 4.2.3 Enforcement of Displacement Boundary Conditions

The displacement boundary conditions are enforced through the use of a penalty method [90]. Consider the constraint equations

$$\mathbf{t} = \mathbf{C}\mathbf{u} - \mathbf{q}, \tag{4.16}$$

where $\mathbf{C}$ is a diagonal matrix containing a value of one at a degree of freedom where a constraint is imposed and zero elsewhere, and $\mathbf{q}$ is a vector containing nodal displacement constraints.

When solving a system of equations

$$\mathbf{K}\mathbf{u} = \mathbf{F}, \tag{4.17}$$

with constraint $\mathbf{t} = \mathbf{0}$, the resulting system is

$$\left[\mathbf{K} + \mathbf{C}^T P^* \mathbf{C}\right] \mathbf{u} = \mathbf{F} + \mathbf{C}^T P^* \mathbf{q}, \tag{4.18}$$

where $P^*$ is a user defined penalty number that is sufficiently large to enforce the constraint, but not large enough to cause an ill-conditioned stiffness matrix. Otherwise, the diagonal entries are zero.

Using this methodology on the current problem, equation 4.6 is modified to

$$\mathbf{f}_e^{\text{ext}} := -\int_{\mathbf{\Omega}^e} \mathbf{B}_e^T \bar{\boldsymbol{\sigma}}^h \mathrm{d}\mathbf{\Omega} + \int_{\mathbf{\Gamma}_q^e} P^* \mathbf{N}_e^T \mathbf{N}_e \left(\mathbf{q} - \mathbf{u}_e\right) \mathrm{d}\mathbf{\Gamma}, \tag{4.19}$$

where $\mathbf{q}$ are element displacement boundary conditions, $\mathbf{u}_e$ are element nodal displacements, and $\mathbf{N_e}$ is a matrix of size $3 \times 24$ whose value for a given node is

$$\mathbf{N}_e^a = \begin{bmatrix} N_a & 0 & 0 \\ 0 & N_a & 0 \\ 0 & 0 & N_a \end{bmatrix}. \tag{4.20}$$

The local stiffness matrix given in equation 4.14 is modified to

$$\mathbf{k}_e|_{n+1}^{(k)} = \int_{\mathbf{\Omega}^e} \mathbf{B}_e^T \left[\frac{\partial \boldsymbol{\sigma}_{n+1}^{(k)}}{\partial \boldsymbol{\varepsilon}_{n+1}^{(k)}}\right] \mathbf{B}_e \mathrm{d}\mathbf{\Omega} + \int_{\mathbf{\Gamma_q^e}} \mathbf{N}_e^T P^* \mathbf{N}_e \mathrm{d}\mathbf{\Gamma}. \tag{4.21}$$

### 4.2.4 Elements and Integration

The type of isoparametric element used in the discretization process is an 8-node bilinear brick element shown in figure 4.3, with nodal locations at $(\xi, \eta, \zeta) = (\pm 1, \pm 1, \pm 1)$. The shape functions, or interpolation functions, have the form

$$N_a\left(\xi, \eta, \zeta\right) = \frac{1}{8}\left(1 + \xi_a \xi\right)\left(1 + \eta_a \eta\right)\left(1 + \zeta_a \zeta\right), \tag{4.22}$$

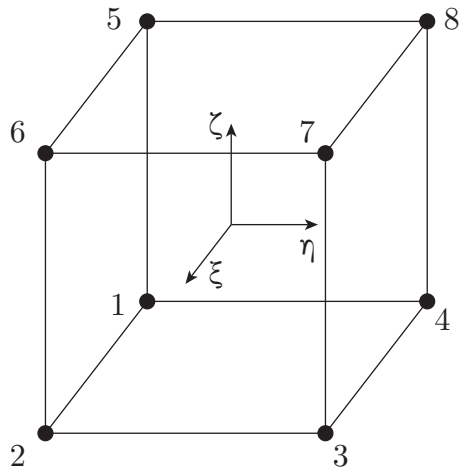


Figure 4.3: Eight Node Brick Element.

where $\xi_a$,$\eta_a$, and $\zeta_a$ are nodal coordinates in isoparametric space. The value of an arbitrary variable $\bar{f}$ within the element is then

$$\bar{f}(\xi,\eta,\zeta) = \sum_{a=1}^{8} N_a(\xi,\eta,\zeta)\,\bar{f}_a, \tag{4.23}$$

where $\bar{f}_a$ are nodal values of $\bar{f}$.

To determine the values of the stiffness matrix and load vector, we need to numerically compute integrals of the form

$$\int_{\mathbf{\Omega}^e} f(\mathbf{x})\,\mathrm{d}\mathbf{\Omega}. \tag{4.24}$$

Evaluating this integral in three-dimensional space over the isoparametric element, we have

$$\int_{\mathbf{\Omega}^e} f(x,y,z)\,\mathrm{d}\mathbf{\Omega} = \int_{-1}^{1}\int_{-1}^{1}\int_{-1}^{1} f(x(\xi,\eta,\zeta), y(\xi,\eta,\zeta), z(\xi,\eta,\zeta))\, j(\xi,\eta,\zeta)\,\mathrm{d}\xi\mathrm{d}\eta\mathrm{d}\zeta, \tag{4.25}$$

where

$$j = \det(\partial\mathbf{x}/\partial\boldsymbol{\xi}) \tag{4.26}$$

is the Jacobian determinant.

Gaussian quadrature is used to numerically evaluate integrals, which takes the

following form in three-dimensional space:

$$\int_{-1}^{1}\int_{-1}^{1}\int_{-1}^{1} g\left(\xi,\eta,\zeta\right) \approx \sum_{l=1}^{n_{int}} g\left(\tilde{\xi}_l,\tilde{\eta}_l,\tilde{\zeta}_l\right) W_l, \tag{4.27}$$

where $n_{int}$ is the number of integration points, $\tilde{\xi}_l$, $\tilde{\eta}_l$ and $\tilde{\zeta}_l$ are the location of integration points, and $W_l$ are weights. In the present work, eight integration points are used in each element.

### 4.2.5 Periodic Boundary Conditions

It is necessary, for reasons discussed in the following chapter, for the boundary conditions to be periodic. This means that opposing faces of a body are required to have identical features and displacements throughout the deformation process. For a portion of the boundary $\Gamma_1$ periodic to $\Gamma_2$, we have

$$\mathbf{u}|_{\Gamma_1} = \mathbf{u}|_{\Gamma_2}. \tag{4.28}$$

A body with periodic boundary conditions can be visualized in figure 4.4. During

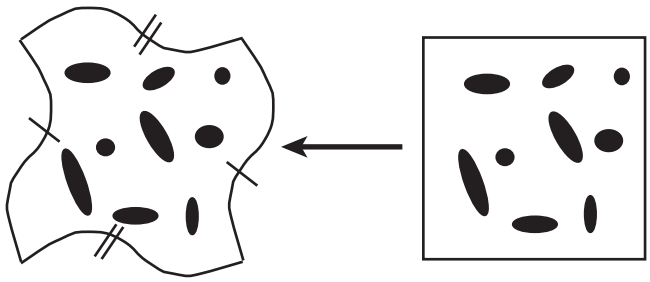

Figure 4.4: A body with periodic boundary conditions in the deformed and undeformed configuration.

the discretization process of a body, enforcement of element and node periodicty is necessary.

Similarly to before, a penalty method is applied to alter the local stiffness matrix and load vector as follows:

$$\begin{aligned} \mathbf{k}_e|_{n+1}^{(k)} &= \textstyle\int_{\mathbf{\Omega}^e} \mathbf{B}_e^T \left[\frac{\partial \boldsymbol{\sigma}_{n+1}^{(k)}}{\partial \boldsymbol{\varepsilon}_{n+1}^{(k)}}\right] \mathbf{B}_e \mathrm{d}\mathbf{\Omega} + \int_{\mathbf{\Gamma}_q^e} \mathbf{N}_e^T P^* \mathbf{N}_e \mathrm{d}\mathbf{\Gamma}, \\ \mathbf{f}_e^{\text{ext}} &:= -\textstyle\int_{\mathbf{\Omega}^e} \mathbf{B}_e^T \bar{\boldsymbol{\sigma}}^h \mathrm{d}\mathbf{\Omega} + \int_{\mathbf{\Gamma}_q^e} P^* \mathbf{N}_e^T \left(\mathbf{N}_e \mathbf{q} - \left(\mathbf{N}_e \mathbf{u}_e - \mathbf{N}_{ep} \mathbf{u}_{ep}\right)\right) \mathrm{d}\mathbf{\Gamma}, \end{aligned} \tag{4.29}$$

where $\mathbf{N_{ep}}$ is the shape function matrix for the periodic element and $\mathbf{u}_{ep}$ is the nodal displacements of the periodic element. Also, define the contribution to the periodic

element's stiffness matrix as

$$\mathbf{k}_{ep}|_{n+1}^{(k)} = \int_{\mathbf{\Gamma}_{\boldsymbol{q}}^{\boldsymbol{e}}} \mathbf{N}_e^T P^* \mathbf{N}_{ep} \mathrm{d}\mathbf{\Gamma}. \tag{4.30}$$

The new global stiffness matrix takes the form

$$\mathbf{K}_{n+1}^{(k)} = \overset{n_{el}}{\underset{e=1}{\mathbf{A}}} \mathbf{k}_e|_{n+1}^{(k)} + \overset{n_{el}}{\underset{e=1}{\mathbf{A}}} \mathbf{k}_{ep}|_{n+1}^{(k)}. \tag{4.31}$$

## 4.3 Conjugate Gradient

The determination of $\Delta\mathbf{u}_{n+1}^{(k+1)}$ in equation 4.13 requires the solution to a system of equations. To do this, a conjugate gradient algorithm is employed as seen in [3] and [90]. The solution steps for solving a system of the form given in equation 4.17 are:

*Box 4: Conjugate Gradient*:

1. For $i = 1$ Select intial guess $\mathbf{u}_1 \Rightarrow \mathbf{r} = \mathbf{F} - \mathbf{K}\mathbf{u}_1 = \mathbf{z}_1$
2. Compute (with $\mathbf{z}_1 = \mathbf{r}_1$)
   $\lambda_1 = \frac{\mathbf{z}_1^T \mathbf{r}_1}{\mathbf{z}_1^T \mathbf{K} \mathbf{z}_1}$
3. Compute $\mathbf{u}_2 = \mathbf{u}_1 + \lambda_1 \mathbf{z}_1$
4. For $i > 1$ compute $\mathbf{r}_i = \mathbf{F} - \mathbf{K}\mathbf{u}_i$
   $\theta_i = -\dfrac{\mathbf{r}_i^T \mathbf{K} \mathbf{z}_{i-1}}{\mathbf{z}_{i-1}^T \mathbf{K} \mathbf{z}_{i-1}}$
   $\mathbf{z}_i = \mathbf{r}_i + \theta_i \mathbf{z}_{i-1}$
   $\lambda_i = \dfrac{\mathbf{z}_i^T \mathbf{r}_i}{\mathbf{z}_i^T \mathbf{K} \mathbf{z}_i}$
5. Compute $\mathbf{u}_{i+1} = \mathbf{u}_i + \lambda_i \mathbf{z}_i$
6. Compute err $:= \frac{\|\mathbf{u}_{i+1} - \mathbf{u}_i\|_{\mathbf{K}}}{\|\mathbf{u}_i\|_{\mathbf{K}}} = \frac{|\lambda_i| \|\mathbf{z}_i\|_{\mathbf{K}}}{\|\mathbf{u}_i\|_{\mathbf{K}}}$
   If err $<$ tol $\Rightarrow$ *Stop*
   If err $\geq$ tol $\Rightarrow$ Go to step 4.

where $\|\{\cdot\}\| = \sqrt{\{\cdot\}^T \mathbf{K} \{\cdot\}}$.

## 4.4 Newton-Raphson Method

In the applications section of this work, it is often necessary to find approximations of a real valued function

$$f(\mathbf{x}) = 0 \tag{4.32}$$

that is dependent on $\mathbf{x}$. The Newton-Raphson method is used for finding successively better approximations to the roots of the function $f(\mathbf{x})$ and has quadratic convergence for non-repeated roots. Starting with an initial guess $\mathbf{x}_0$, the updated guess is

$$\mathbf{x}_{n+1} = \mathbf{x}_n - \left[\frac{\partial f(\mathbf{x})}{\partial \mathbf{x}}\right]_n^{-1} f(\mathbf{x}_n) \tag{4.33}$$

and the solution is considered to converge when $\|\mathbf{x}_{n+1} - \mathbf{x}_n\| < \text{tol}$. Further information can be found in [40] and [6].

# Chapter 5

# Multiscale Modeling

Consider a heterogeneous body with two length scales, shown in 5.1, such that $H >> h$. If one were to attempt to perform a direct numerical simulation of a macroscopic response while incorporating all of the microscale details, an extremely fine spatial discretization would be needed. The resulting system of equations would contain a vast number of unknowns and be beyond the capacity of computing machines for the forseeable future.

Rather than discretizing every detail of the microstructure within the macro problem, the use of a homegnized material model is employed. For a complete account of the subject, refer to Zohdi [90], Aboudi [1], Hashin [32], Mura [58], Nemat-Nasser [59], and Galvanetto [24].

The problem is resolved into two separate scales: the macro-scale and a Representative Volume Element (RVE), which characterizes the micro-scale at a single point. Most practical computational homogenization approaches make an assumption

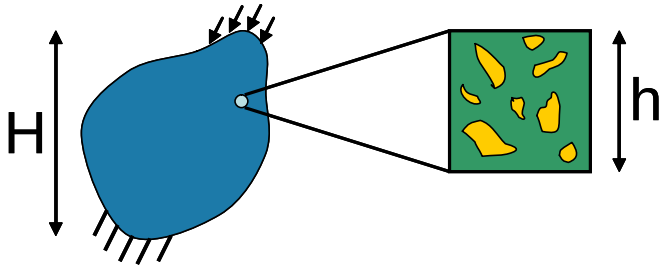


Figure 5.1: Illustration of a heterogeneous body being approximated by a Representative Volume Element (RVE).

of local periodicity on the RVE instead of global periodicity, which allows the modeling of effects of a non-uniform distribution of the microstructure on the macroscopic response.

The purpose of this scheme is to use the RVE as a way to obtain the material tangent at every location in the macrostructure. This tangent is used to solve the macro problem, obtaining stresses and strains point-wise. The resulting deformation gradient can then be mapped back onto the RVE in order to obtain a solution at the micro level. This scheme can be visualized in 5.2. A potential drawback of this model is that the use of an orthotropic RVE will introduce orthotropic tendencies into the material response. However, isotropic unit cells such as a three dimensional hexagon is often cumbersome to implement.

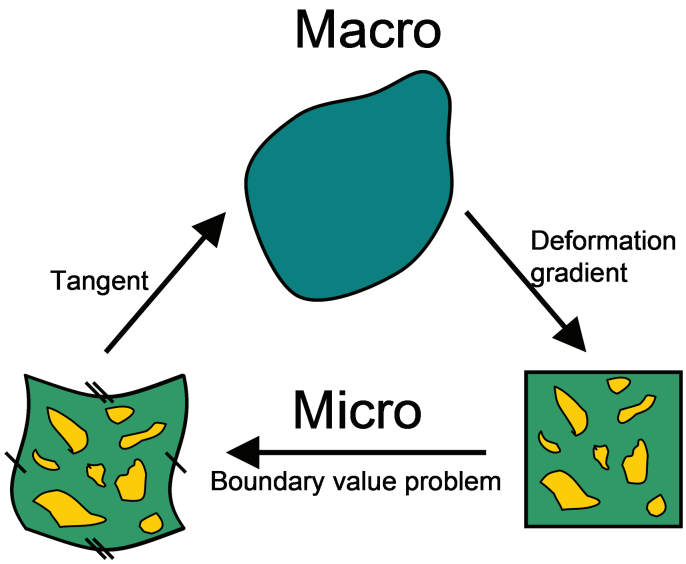


Figure 5.2: Computational homogenization scheme.

## 5.1 Linear Elasticity

Consider the case of lienar elasticity. For microheterogeneous materials, the mechanical properties are characterized by a spatially variable tensor $\mathbf{C}$, referred to as the elasticity tensor. In order to characterize the homogized effective macroscopic response, we seek the fourth order tensor $\mathbf{C}^*$, referred to as the effective elasticity tensor over the RVE, which fulfills the relation

$$\langle \boldsymbol{\sigma} \rangle_{\boldsymbol{\Omega}} = \mathbf{C}^* : \langle \boldsymbol{\varepsilon} \rangle_{\boldsymbol{\Omega}} \,, \tag{5.1}$$

where : is an inner product operator and

$$\langle \cdot \rangle_{\mathbf{\Omega}} := \frac{1}{|\mathbf{\Omega}|} \int_{\mathbf{\Omega}} \cdot \, \mathrm{d}\mathbf{\Omega}, \tag{5.2}$$

where $\mathbf{\Omega}$ represents the domain of the RVE and $|\mathbf{\Omega}|$ is the volume of the domain. It should be noted that the effective quantity $\mathbf{C}^*$ is not a material property, but instead a relation between averages. In the case where heterogeneties are randomly distributed and randomly oriented, the effective response $\mathbf{C}^*$ is assumed to be isotropic and there are only two independent constants in $\mathbf{C}^*$, having the following relation:

$$\mathbf{C}^* \langle \boldsymbol{\varepsilon} \rangle_{\mathbf{\Omega}} = 3\kappa^* \langle \frac{\mathrm{tr}\boldsymbol{\varepsilon}}{3} \rangle_{\mathbf{\Omega}} \mathbf{1} + 2\mu^* \langle \boldsymbol{\varepsilon}' \rangle_{\mathbf{\Omega}}, \tag{5.3}$$

where the effective bulk and shear moduli are given by $3\kappa^* := \langle \frac{\mathrm{tr}\boldsymbol{\sigma}}{3} \rangle_{\mathbf{\Omega}} / \langle \frac{\mathrm{tr}\boldsymbol{\varepsilon}}{3} \rangle_{\mathbf{\Omega}}$ and $2\mu^* := \sqrt{\langle \boldsymbol{\sigma}' \rangle_{\mathbf{\Omega}} : \langle \boldsymbol{\sigma}' \rangle_{\mathbf{\Omega}} / \langle \boldsymbol{\varepsilon}' \rangle_{\mathbf{\Omega}} : \langle \boldsymbol{\varepsilon}' \rangle_{\mathbf{\Omega}}}$, where $tr\boldsymbol{\varepsilon} = \varepsilon_{ii}$ and $\boldsymbol{\varepsilon}' = \boldsymbol{\varepsilon} - \frac{1}{3}(\mathrm{tr}\boldsymbol{\varepsilon})\mathbf{1}$ is the deviatoric strain and similarly $\boldsymbol{\sigma}'$ is the deviatoric stress. The reader is directed to the additional works of Torquato [77, 78, 79, 80, 81] for additional details on effective properties.

Classical approaches have sought to bound effective responses. The initial analysis of the effective mechanical properties of microheterogeneous solds was performed by Voigt [83], where he assumed that the strain field within a sample of the heterogeneous material was uniform, leading to $\langle \mathbf{C} \rangle_{\mathbf{\Omega}}$ as the approximate effective property of an RVE. Reuss [68] later approximated the stress fields within the heterogeneous material as uniform, leading to $\langle \mathbf{C}^{-1} \rangle_{\mathbf{\Omega}}^{-1}$ as the approximation of the effective property. A fundamental result, shown by Hill [35], is

$$\left\langle \mathbf{C}^{-1} \right\rangle_{\mathbf{\Omega}}^{-1} \leq \mathbf{C}^* \leq \left\langle \mathbf{C} \right\rangle_{\mathbf{\Omega}}, \tag{5.4}$$

which means that the Voight and Reuss fields provide two microfield extremes. In the case of a two-phase microstructure with each phase being isotropic, equation 5.4 reduces to

$$\frac{1}{\frac{v_2}{\kappa_2} + \frac{1-v_2}{\kappa_1}} \leq \kappa^* \leq v_2\kappa_2 + (1-v_2)\,\kappa_1, \tag{5.5}$$

and

$$\frac{1}{\frac{v_2}{\mu_2} + \frac{1-v_2}{\mu_1}} \leq \mu^* \leq v_2\mu_2 + (1-v_2)\,\mu_1, \tag{5.6}$$

where $\kappa$ is the bulk modulus, $\mu$ is the shear modulus, $v_2$ is the phase 2 volume fraction.

Hashin and Shtrikman [32] [33] introduced the tighter bounds

$$\kappa_1 + \frac{v_2}{\frac{1}{\kappa_2-\kappa_1} + \frac{3(1-v_2)}{3\kappa_1+4\mu_1}} \leq \kappa^* \leq \kappa_2 + \frac{1-v_2}{\frac{1}{\kappa_1-\kappa_2} + \frac{3v_2}{3\kappa_2+4\mu_2}}, \tag{5.7}$$

and

$$\mu_1 + \frac{v_2}{\frac{1}{\mu_2-\mu_1} + \frac{6(1-v_2)(\kappa_1+2\mu_1)}{5\mu_1(3\kappa_1+4\mu_1)}} \leq \mu^* \leq \mu_2 + \frac{1-v_2}{\frac{1}{\mu_1-\mu 2} + \frac{6v_2(\kappa_2+2\mu_2)}{5\mu_2(3\kappa_2+4\mu_2)}}, \tag{5.8}$$

where $\kappa_2 \geq \kappa_1$ and $\mu_2 \geq \mu 1$.

### 5.1.1 Concetration Tensors

The load carried by each phase in the microstructure can be characterized through use of concentration tensors, which provide a measure of the deviation away from the mean fields throughout the material. The averages of an arbitrary quantity can be decomposed over $\Omega$ into averages over each of the phases in the following manner:

$$\langle\cdot\rangle_{\mathbf{\Omega}} = \frac{1}{|\mathbf{\Omega}|}\sum_{i=1}^{n}\int_{\mathbf{\Omega}_i}\cdot \mathrm{d}\mathbf{\Omega} = \sum_{i=1}^{n} v_i \langle\cdot\rangle_{\mathbf{\Omega}_i} \tag{5.9}$$

where $\mathbf{\Omega}_i$ represents the domain of the i-th phase. For the case with a single particle phase and a matrix phase, this equation becomes

$$\langle\cdot\rangle_{\mathbf{\Omega}} = v_1 \langle\cdot\rangle_{\mathbf{\Omega}_1} + v_2 \langle\cdot\rangle_{\mathbf{\Omega}_2}. \tag{5.10}$$

Using this this decomposition, the average stress over the entire domain can be written as

$$\begin{aligned}
\langle\boldsymbol{\sigma}\rangle_{\mathbf{\Omega}} &= v_1\langle\boldsymbol{\sigma}\rangle_{\mathbf{\Omega}_1} + v_2\langle\boldsymbol{\sigma}\rangle_{\mathbf{\Omega}_2} \\
&= v_1\mathbf{C}_1 : \langle\boldsymbol{\varepsilon}\rangle_{\mathbf{\Omega}_1} + v_2\mathbf{C}_2 : \langle\boldsymbol{\varepsilon}\rangle_{\mathbf{\Omega}_2} \\
&= \mathbf{C}_1 : (\langle\boldsymbol{\varepsilon}\rangle_{\mathbf{\Omega}} - v_2\langle\boldsymbol{\varepsilon}\rangle_{\mathbf{\Omega}_2}) + v_2\mathbf{C}_2 : \langle\boldsymbol{\varepsilon}\rangle_{\mathbf{\Omega}_2} \\
&= (\mathbf{C}_1 + v_2(\mathbf{C}_2 - \mathbf{C}_1) : \mathbf{c}) : \langle\boldsymbol{\varepsilon}\rangle_{\mathbf{\Omega}},
\end{aligned} \tag{5.11}$$

where the strain concentration tensor $\mathbf{c} := \left(\frac{1}{v_2}(\mathbf{C}_2 - \mathbf{C}_1)^{-1} : (\mathbf{C}^* - \mathbf{C}_1)\right)$, with $\mathbf{c} : \langle\boldsymbol{\varepsilon}\rangle_{\mathbf{\Omega}} = \langle\boldsymbol{\varepsilon}\rangle_{\mathbf{\Omega}_2}$. The strain concentration tensor $\mathbf{c}$ relates the average strain over the particle phase to the average strain over all phases.

Similarly, for the variation in the stress, $\mathbf{c} : \mathbf{C}^{*-1} : \langle\boldsymbol{\sigma}\rangle_{\mathbf{\Omega}} = \mathbf{C}_2^{-1} : \langle\boldsymbol{\sigma}\rangle_{\mathbf{\Omega}_2}$, which reduces to $\mathbf{C}_2 : \mathbf{c} : \mathbf{C}^{*-1} : \langle\boldsymbol{\sigma}\rangle_{\mathbf{\Omega}} := \overline{\mathbf{c}} : \langle\boldsymbol{\sigma}\rangle_{\mathbf{\Omega}} = \langle\boldsymbol{\sigma}\rangle_{\mathbf{\Omega}_2}$. $\overline{\mathbf{c}}$ is known as the stress concentration tensor, and relates the average stress in the particle phase to the average stress over all phases. In the case of isotropy,

$$\overline{c}_\kappa := \frac{1}{v_2}\frac{\kappa_2}{\kappa^*}\frac{\kappa^* - \kappa_1}{\kappa_2 - \kappa_1} \quad \text{and} \quad \overline{c}_\mu := \frac{1}{v_2}\frac{\mu_2}{\mu^*}\frac{\mu^* - \mu_1}{\mu_2 - \mu_1}, \tag{5.12}$$

where $\overline{c}_\kappa\langle\frac{tr\boldsymbol{\sigma}}{3}\rangle_{\mathbf{\Omega}} = \langle\frac{tr\boldsymbol{\sigma}}{3}\rangle_{\mathbf{\Omega}_2}$ and $\overline{c}_\mu\langle\boldsymbol{\sigma}'\rangle_{\mathbf{\Omega}} = \langle\boldsymbol{\sigma}'\rangle_{\mathbf{\Omega}_2}$. The microstress fields are minimally distorted when $\overline{c}_\kappa = \overline{c}_\mu = 1$ since there are no stress concentrations in a

homogeneous material. For the matrix,

$$\langle \boldsymbol{\sigma} \rangle_{\boldsymbol{\Omega}_1} = \frac{\langle \boldsymbol{\sigma} \rangle_{\boldsymbol{\Omega}} - v_2 \langle \boldsymbol{\sigma} \rangle_{\boldsymbol{\Omega}_2}}{v_1} = \frac{\langle \boldsymbol{\sigma} \rangle_{\boldsymbol{\Omega}} - v_2 \overline{\mathbf{c}} : \langle \boldsymbol{\sigma} \rangle_{\boldsymbol{\Omega}}}{v_1} = \frac{(\mathbf{1} - v_2 \overline{\mathbf{c}}) : \langle \boldsymbol{\sigma} \rangle_{\boldsymbol{\Omega}}}{v_1} := \overline{\overline{\mathbf{c}}} : \langle \boldsymbol{\sigma} \rangle_{\boldsymbol{\Omega}}. \tag{5.13}$$

In the case of isotropy,

$$\overline{\overline{c}}_\kappa := \frac{1}{v_1}(1 - v_2 \overline{c}_\kappa) \quad \text{and} \quad \overline{\overline{c}}_\mu := \frac{1}{v_1}(1 - v_2 \overline{c}_\mu). \tag{5.14}$$

### 5.1.2 Direct Evaluation of Effective Properties

As computational ability progresses, the direct determination of the effective properties becomes more realistic. In order to compute these properties, six different loading conditions can be applied to determine the effective elasticity tensor. The linear stress-strain elastic relation can be written as

$$\begin{bmatrix} \sigma_x \\ \sigma_y \\ \sigma_z \\ \tau_{xy} \\ \tau_{yz} \\ \tau_{zx} \end{bmatrix} = \begin{bmatrix} C_{11} & C_{12} & C_{13} & C_{14} & C_{15} & C_{16} \\ C_{21} & C_{22} & C_{23} & C_{24} & C_{25} & C_{26} \\ C_{31} & C_{32} & C_{33} & C_{34} & C_{35} & C_{36} \\ C_{41} & C_{42} & C_{43} & C_{44} & C_{45} & C_{46} \\ C_{51} & C_{52} & C_{53} & C_{54} & C_{55} & C_{56} \\ C_{61} & C_{62} & C_{63} & C_{64} & C_{65} & C_{66} \end{bmatrix} \begin{bmatrix} \epsilon_x \\ \epsilon_y \\ \epsilon_z \\ \gamma_{xy} \\ \gamma_{yz} \\ \gamma_{zx} \end{bmatrix} \tag{5.15}$$

where the left column represents the three-dimensional stress state of a material point, the right column represents the strain state of a material point, and an elasticity tensor with thirty six constants connects the two. It can be seen that if only one non-zero value of the strain components is imposed, computation of the stress state will determine the corresponding column of the elasticity tensor. To extract the effective properties of the RVE, six different average strain states over the domain are imposed, and the corresponding average stress states are calculated using the finite element scheme described in chapter 4 to construct the effective elasticity tensor. Note that for the linear case the properties of the RVE only need to be determined once since the material behavior is independent of the stress and strain state.

Once the effective material properties of the RVE are obtained, they can be used to solve the macro-scale model directly, resulting in a stress-strain distribution at the macro level. This resulting stress state can then be applied back onto the RVE in order to obtain the stress and strain distribution present in the micro-scale.

## 5.2 Infinitessimal Plasticity

When considering nonlinear multi-scale models, the material behavior at a point is dependent on its corresponding stress and strain (or strain increment) states. In

order to account for this behavior in the hierarchical model, the effective properties of the RVE can be determined point-wise at the current stress and strain state. In the current model, the effective properties are not actually calculated. Instead, the deforming body is updated according to its elasto-plastic constitutive behavior described in chapter 4.

When using a finite element model to analyze the macroscale, the effective properties need to be determined at every integration point. Performing a finite element analysis at every integration point in the body can be computationally expensive; therefore, material points with near equal stress states are approximated by a single RVE. Consider the body in figure 5.3, subdivided into smaller domains. The effective properties can be calculated once within each subdomain, and determined elsewhere through interpolation.

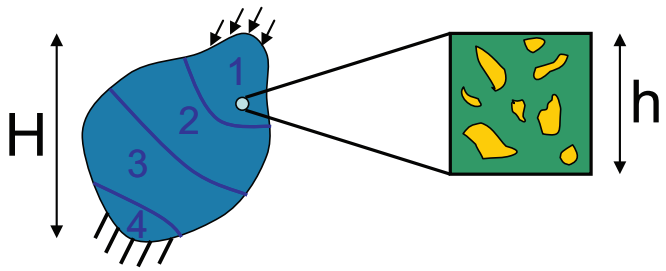


Figure 5.3: Illustration of a heterogeneous body being subdivided into domains approximated by their own RVEs.

An additional complication in the nonlinear case is that since the effective properties are dependent on the stress state of the macro level, effective properties need to be recomputed for every load increment, whereas they can be reused in when the behavior is linear and temperature is fixed.

## 5.3 Morphology of Microstructure

It has been established that the effective properties of a heterogeneous material are dependent on both the properties of each phase as well as the microstructural layout [36] [74]. In addition, these effective material properties are dependent on complex interactions between phases, which is determined by the microstructural information, as well as the volume fraction of each phase [80] [44].

### 5.3.1 Non-Periodic Microstructure

Heterogeneous microstructures are typically non-periodic, and therefore the chosen size of the RVE is critical in regards to the accuracy of the RVE's characterization

of the microstructure as well as the computation time needed to evaluate the RVE's effective properties. For a RVE to be considered a suitable representation of the microstructure, it must statistically characterize the behavior of the material.

In order to obtain an accurate description of the morphology of a heterogenous microstructure, n-point probability functions can be employed to determine the microstructure characterization of an m-phased composite. A detailed description of n-point probability functions for two-phased spherical composites can be found in [80]. For these composites, a sample size of roughly 100 particles are needed for an accurate statisical representation of the microstructure. A lower sample size would result in inaccurate effective properties, but a much larger sample size would require many more degrees of freedom during the numerical evaulation of the RVE's effective properties.

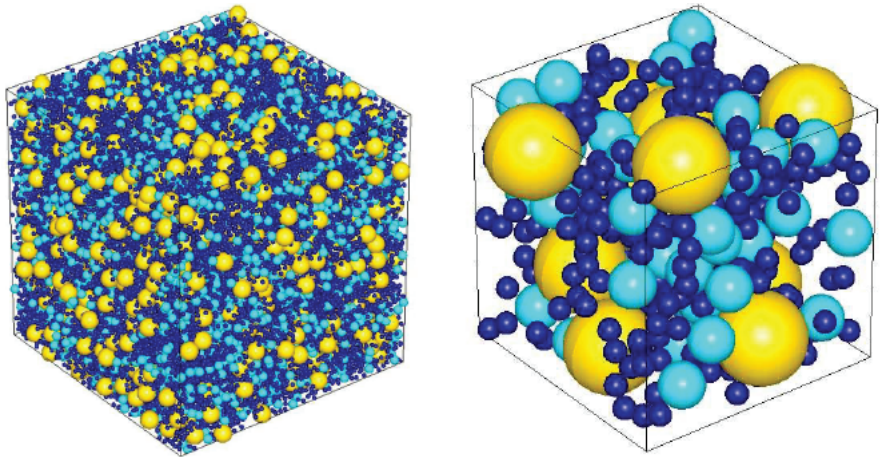

Figure 5.4: Original material sample of a trimodal particle pack at 40% packing fraction and reconstructed periodic unit cell.

Collins and Matouš [10] have developed a process to construct optimally sized RVEs for particulate composites based on using a genetic algorithm to match 1- and 2-point probability functions between the original material sample and the RVE. In figure 5.4, a trimodal material sample consisting of 50,000 particles at a 40% packing fraction is considered. It would be computationally infeasible to use the entire sample as a RVE, but after using the algorithm developed, only 381 particles are necessary for the sample to be considered statistically representative.

This method of creating periodic unit cells (PUCs) can be applied in a similar fasion for a variety of heterogeneous microstructures, including non-ellipsoidal phases and voids.

### 5.3.2 Periodic Microstructure

In the case where the heterogeneities within a microstructure are in an array, the choice of RVE is often obvious and it becomes unnecessary to go through the proceses described above. For example, consider the fibrous composite in figure 5.5. It is clear that the proper choice of RVE is a single hexagon, although it is often simpler to choose a rectangular domain. It should be noted that accuracy within a multiscale model decreases as the difference in lengthscales between the macro and micro levels diminishes.

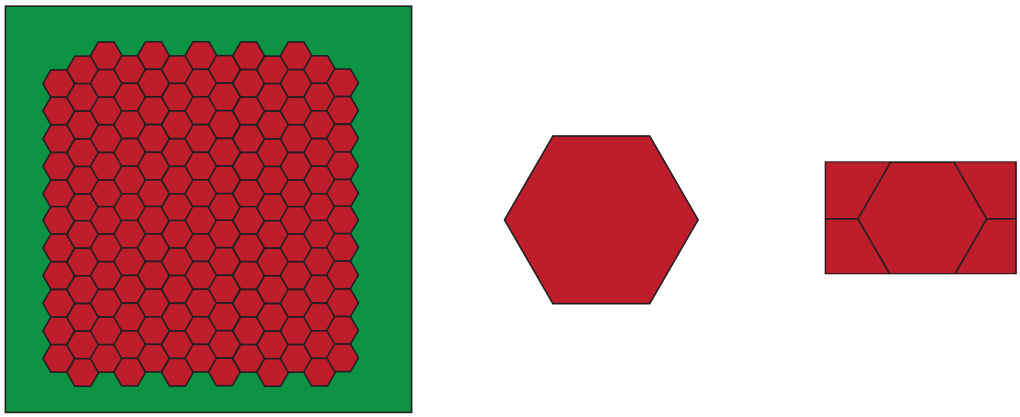

Figure 5.5: A fibrous composite and two simple choices for a RVE.

# Chapter 6

# Application in a Magnet

## 6.1 A Simple RRP Strand

The multiscale method described in the chapter 5 can be applied to a single strand, as shown in figure 6.1. In this model, the filaments are replaced by a single homogeneous material, whose roperties will be determined by an RVE composed of $Nb_3Sn$ filaments surrounded by copper with bronze cores. This RVE is taken to be a 3D periodic unit cell (PUC), indicating that the X, Y, and Z boundary faces remain periodic throughout the deformation process, although it should be noted that this approximation is not exact.

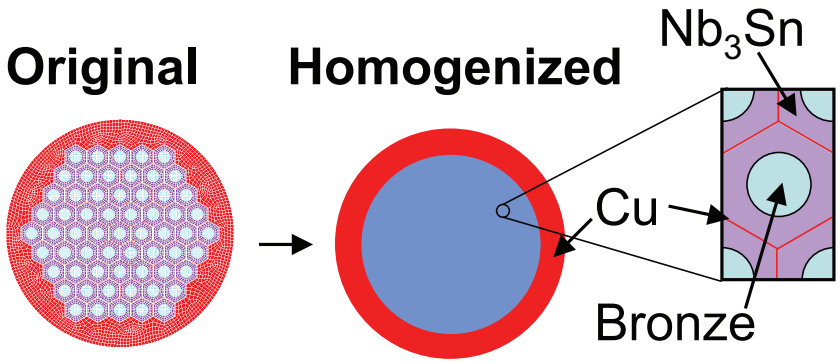


Figure 6.1: Homogenization of a RRP Strand.

As a simplification, the homogenized strand is treated as axisymmetric. The reasoning for this treatment is that if the strand is subjected to a change in temperature or an axisymmmetric load, the resulting stress inside the homogenized core will be uniform, requiring only one RVE to compute the effective behavior. In addition, it is assumed that there is no twist along the axial direction of the strand.

## 6.2 Test Case 1: Cooldown from 300 K to 4.2 K

### 6.2.1 Implementation

The macroscale solution is found by decomposing the outer portions of the strand into two seperate problems and then enforcing continuity in the displacements. This process can be visualized in figure 6.2, where $p$ is a radial pressure, $\sigma$ is the axial stress, and $\delta$ is the displacement.

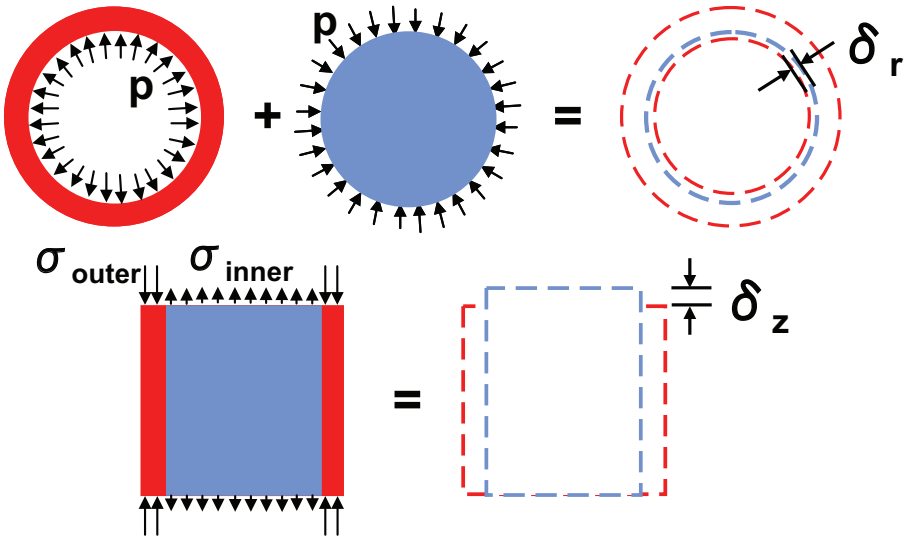


Figure 6.2: Decomposition of Strand in Radial and Axial Directions for Macroscale Solution.

At every loading step, continuity will be enforced by finding the pressures $p$ and $\sigma_{\text{inner}}$ such that the resulting gaps $\delta_r$ and $\delta_z$ approach zero. This is done numerically using a Newton-Raphson method described in 4.4, and the update is given by

$$\begin{Bmatrix} p^{n+1} \\ \sigma^{n+1}_{\text{inner}} \end{Bmatrix} = \begin{Bmatrix} p^{n} \\ \sigma^{n}_{\text{inner}} \end{Bmatrix} - \begin{bmatrix} \frac{\partial \delta_r}{\partial p} & \frac{\partial \delta_r}{\partial \sigma_{\text{inner}}} \\ \frac{\partial \delta_z}{\partial p} & \frac{\partial \delta_z}{\partial \sigma_{\text{inner}}} \end{bmatrix}^{-1}_{n} \begin{Bmatrix} \delta_r \\ \delta_z \end{Bmatrix}_{n} \tag{6.1}$$

The stress tensor in the inner homogenized region of the strand takes the form

$$\boldsymbol{\sigma}_{\text{inner}} = \begin{bmatrix} -p & 0 & 0 \\ 0 & -p & 0 \\ 0 & 0 & \sigma_{\text{inner}} \end{bmatrix}, \tag{6.2}$$

and by enforcing equilibrium in the axial direction and assuming that the outer copper

region is thin walled, the corresoponding outer stress tensor is

$$\boldsymbol{\sigma}_{\text{inner}} = \begin{bmatrix} 0 & 0 & 0 \\ 0 & \frac{pR}{t} & 0 \\ 0 & 0 & -\frac{A_{\text{inner}}}{A_{\text{outer}}}\sigma_{\text{inner}} \end{bmatrix}, \tag{6.3}$$

where $R$ is the radius of the strand, $t$ is the thickness of the copper region, and $A$ is the cross sectional area.

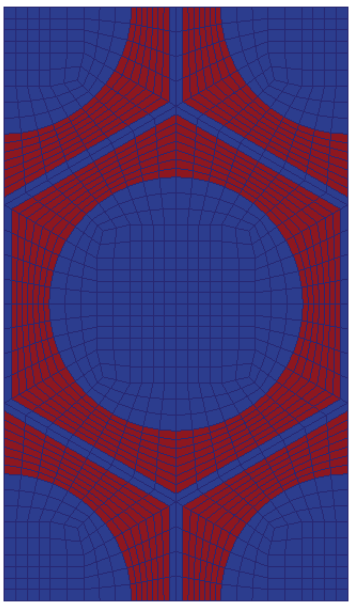

Figure 6.3: A Sample RVE Mesh.

The strain in the inner region of the strand is computed by discretizing the RVE into finite elements and numerically calculating the average strain using the methodology given in previous chapters, whereas the strain in the outer region can be determined directly. A sample RVE mesh can be seen in figure 6.3, where red elements represent $Nb_3Sn$ and blue elements represent copper.

Since the average strain is being computed within the RVE due to an applied average stress, equilibrium over the RVE is enforced using the following Newton-Raphson method:

$$\begin{aligned} \mathbf{f}\left(\bar{\boldsymbol{\varepsilon}}\right) &= \tfrac{1}{V}\int_{\boldsymbol{\Omega}} \boldsymbol{\sigma}\left(\bar{\boldsymbol{\varepsilon}}\right) \mathrm{d}\boldsymbol{\Omega} - \bar{\boldsymbol{\sigma}} = \mathbf{0}, \\ \bar{\boldsymbol{\varepsilon}}_{n+1} &= \bar{\boldsymbol{\varepsilon}}_n - \left[\frac{D\mathbf{f}(\bar{\boldsymbol{\varepsilon}})}{D\bar{\boldsymbol{\varepsilon}}}\right]_n^{-1} \mathbf{f}\left(\bar{\boldsymbol{\varepsilon}}_n\right), \end{aligned} \tag{6.4}$$

where $\bar{\boldsymbol{\sigma}}$ is the average stress tensor applied over the RVE and $\bar{\boldsymbol{\varepsilon}}$ is the resulting average strain tensor.

Deformations are taken to be infinitesimal and the initial residual stress at 300 K will be taken as zero. Ten temperature loading steps are used to bring the strand to 4.2 K. The volume fraction of $Nb_3Sn$ in the RVE is 50

### 6.2.2 Results

The strain and stress in the inner and outer regions of the strand can be seen in figure 6.4 and 6.5 respectively.

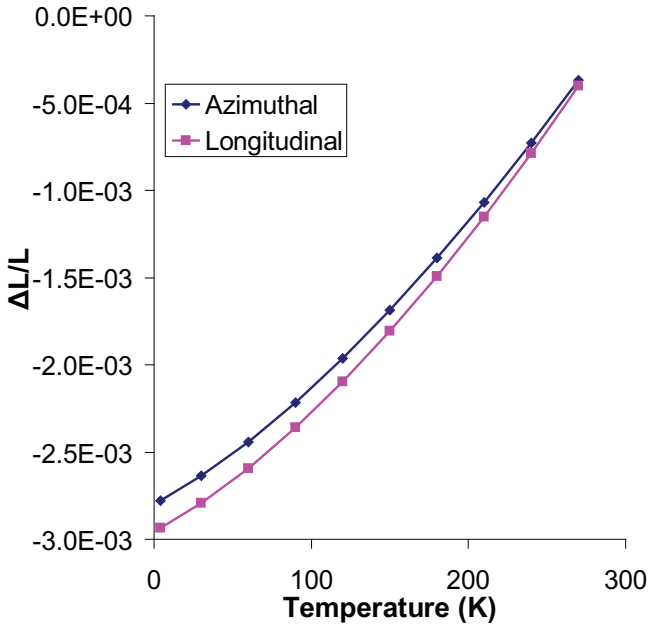


Figure 6.4: Strain Present in Macro-level of Strand Due to a Cooldown from 300 K to 4.2 K.

It can be seen that at 4.2 K there is a decrease in length of the strand corresponding to -0.293 % strain. Similarly, there is a decrease in the azimuthal strain, and therefore radial strain, at 4.2 K corresponding to -0.277 %. These changes in length are noticeably nonlinear, indicating that there is plastic deformation occuring in the outer copper sleeve.

The stress in the outer copper region is tensile, whereas the inner homogenized region experiences an average compressive stress. The average radial and axial stresses in the homogenized region at 4.2 K are -8.0 MPa and -17.8 MPa, respectively.

Determination of the stress in the $Nb_3Sn$ filaments can be accomplished by examining the FEM solution of the RVE at 4.2 K. This model uses 8,526 degrees of freedom.

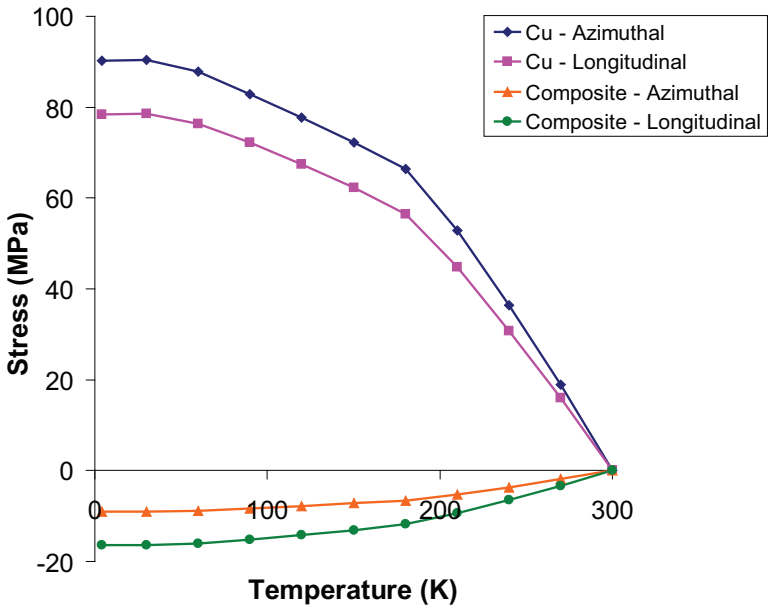


Figure 6.5: Average Stress Present in Inner and Outer Regions of the Strand at the Macro-level Due to a Cooldown from 300 K to 4.2 K.

The von Mises stress in the RVE is shown on the left in figure 6.6. The magnitude of the stress in the individual phases is much larger than the average values calculated at the macro level, with a peak stress of 209 MPa occuring in the $Nb_3Sn$ phase. The elastic strains in the axial direction iside the RVE are shown in the middle of figure 6.6. The copper is in tension, whereas the $Nb_3Sn$ experiences an axial compression of -0.1 %. The plastic strain in the RVE is shown on the right in figure 6.6. Material flow only occurs in the regions surrounding the filaments. The bronze cores do not deform plastically, however, since they are being loaded hydrostatically.

### 6.2.3 Numerical Simulation of Full Strand

In order to guage the validity of the multiscale model, a cooldown is performed numerically on the fully discretized model of a strand using ANSYS®Mechanical, Release 14.0. This model contains 173,382 degrees of freedom, approximately 20 times more than used in the multiscale model. Von Mises stress contours of the strand are shown in figure 6.7.

Although the maximum and minimum values are different than those computed by the multiscale process, these values are located in the outermost filaments. To get an accurate comparison, the inner region of the strand is examined. When the outermost filaments are taken out of consideration, the maximum value of the stress

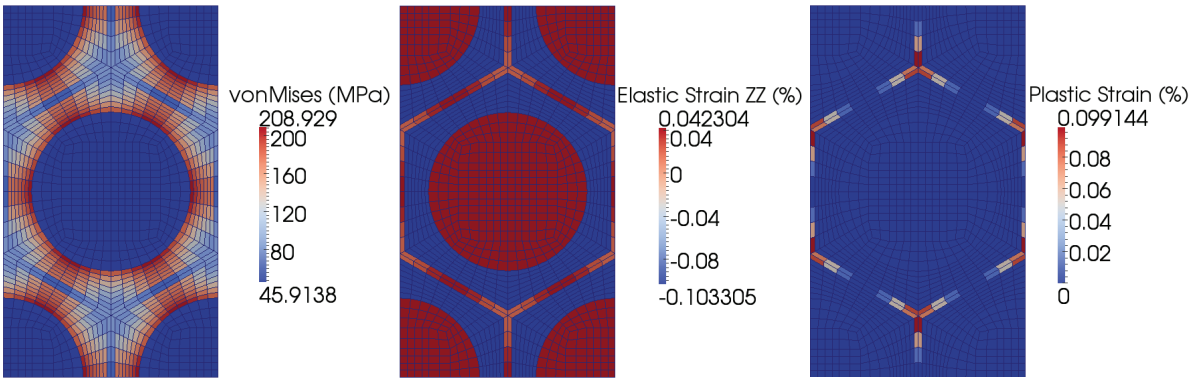


Figure 6.6: Von Mises Stress, Axial Elastic Strain, and Plastic Strain in RVE Due to a Cooldown from 300 K to 4.2 K.

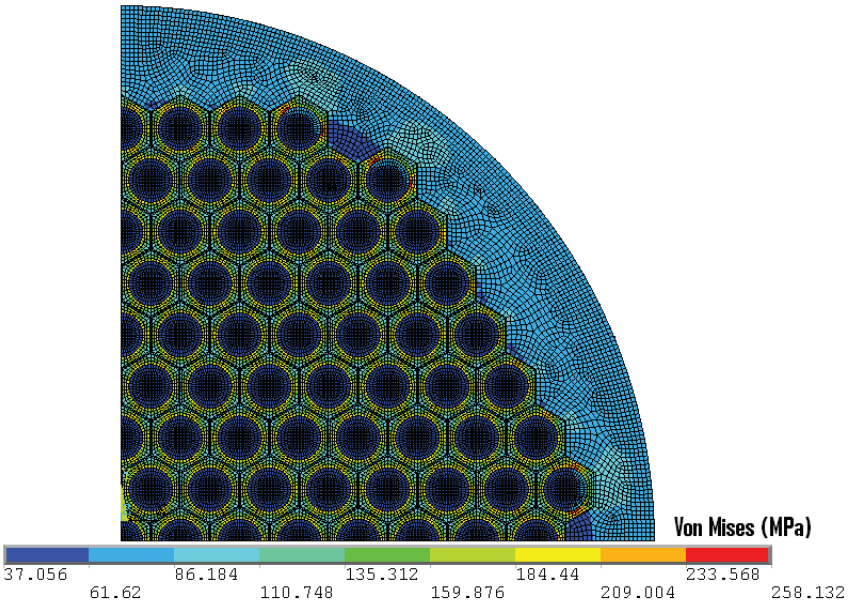


Figure 6.7: Von Mises Stress in Strand Due to a Cooldown from 300 K to 4.2 K.

in the $Nb_3Sn$ phase is 217 MPa, which is similar to the solution found using the hierarchical model.

## 6.3 Alternative Model of the Macroscale

Although it is convenient to use a thin-walled pressure vessel like model at the macroscale, not all strand configurations share this trait. An alternative implementation is described below.

### 6.3.1 RVE

The RVE is again modeled as a 3D periodic cell. However, instead of applying an average stress to the RVE, finding the average strain and iterating using a Newton-Raphson method, we instead apply the average strain tensor to the RVE. The material tangent is obtained numerically about the current strain state by performing additional infinitesimal deformations in each direction and computing the corresponding change in stress. Solutions within the unit cell are again determined through use of the finite element procedure discussed in chapter 4.

### 6.3.2 Macrostructure

Taking into account that future work will incorporate higher hierarchical levels, the strand level is treated as a periodic unit cell as well. The mesh of a general homogenized strand is shown in figure 6.8, where blue is copper, salmon is the homogenized material, and red is a soft, fictitious material.

In order to create a periodic structure at the mesh level, a soft material is added to the exterior of the strand body. In the current work this material is soft enough to provide neglible effects on the strand, but in the future the properties can be altered to represent the epoxy present within impregnated Rutherford cables.

Since periodic boundary conditions are used on the macrostructure as well as the microstructure, equilibrium must be enforced over the macro domain using equation 6.4.

## 6.4 Test Case 2: Cooldown from 480 K to 4.2 K

During the heat treatment process of $Nb_3Sn$ based strands, the temperature is gradually reduced from reaction temperature at 920 K to room temperature. Since annealing occures at approximately 480 K, the individual RRP strand is assumed to be in a stress free configuration at this temperature. The same geometry from the previous example is used.

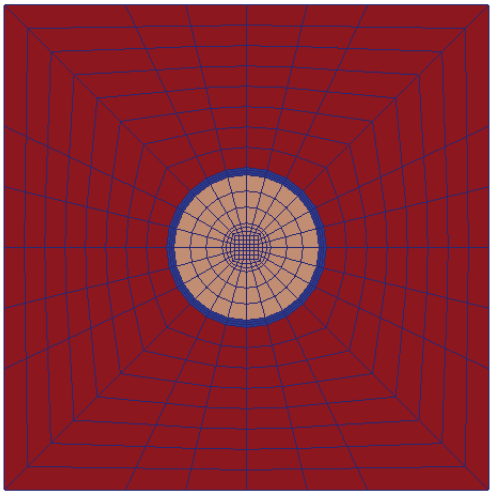

Figure 6.8: Mesh of a Homogenized Strand.

### 6.4.1 Results

Plots of the axial strain and stress of the homogenized strand at 4.2 K can be seen in figure 6.9. When compared to the previous case, it can be seen that the strand

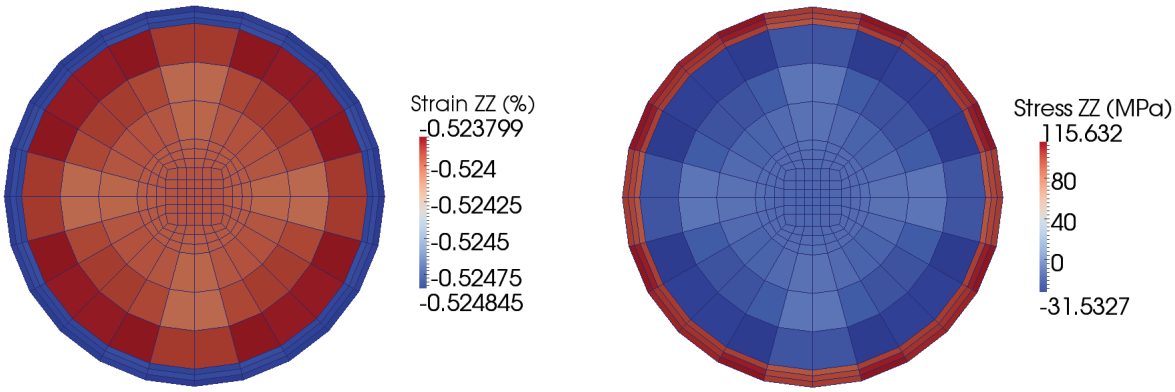


Figure 6.9: Axial Strain and Stress of a Homogenized Strand at 4.2 K.

shortened by an additional -.23 %. Similarly, the axial stress in the homogenized region approximately doubled. It can be noted, that although axisymmetric, use of periodic boundary conditions has introduced orthotropy into the system.

The von Mises stress, the Axial Elastic strain, and the Plastic strain in the RVE is shown in figure 6.10. Compared to the previous case, it can be seen that the magnitude of all values have increased drastically, indicating that the temperature in which the strand has a stress free configuration is critical.

## 6.5 A More Complicated RRP Strand

In this section, a strand containing a copper core is considered, as shown in figure 6.11. This geometry, although more complicated, is more representative of a strand used within an accelerator magnet.

### 6.5.1 Strand Geometry

The strand used in the simulation is a 0.9 mm diameter 45 % Cu 108/127 RRP strand shown in figure 6.12. The corresponding macroscale and RVE are shown in figure 6.13. The axisymmetric geometry in the macroscale model is produced by enforcing that the cross sectional area of the subelements is equal to the coaxial hoogenized region.

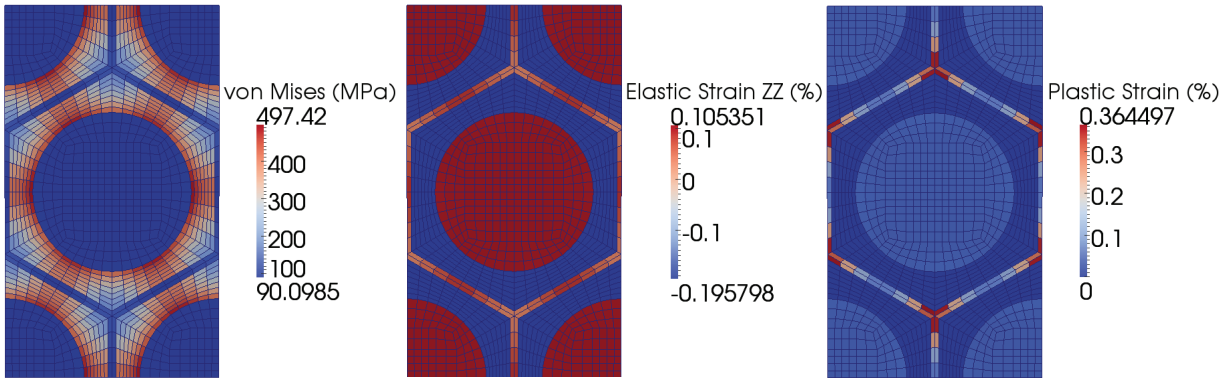


Figure 6.10: Von Mises Stress, Axial Elastic Strain, and Plastic Strain in RVE Due to a Cooldown from 300 K to 4.2 K.

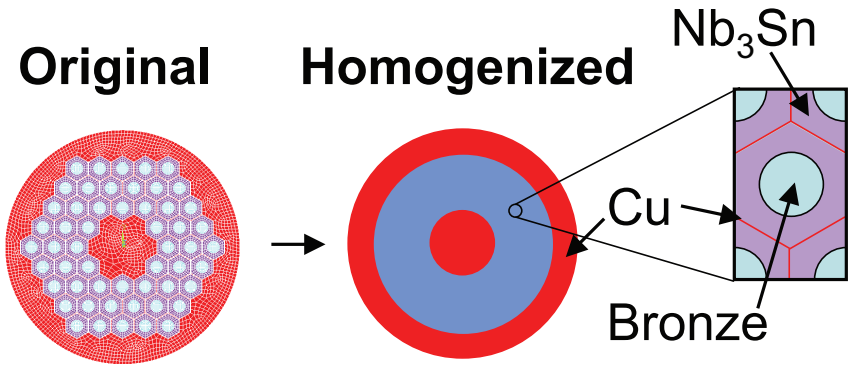


Figure 6.11: Homogenization of a RRP Strand with a Copper Core.

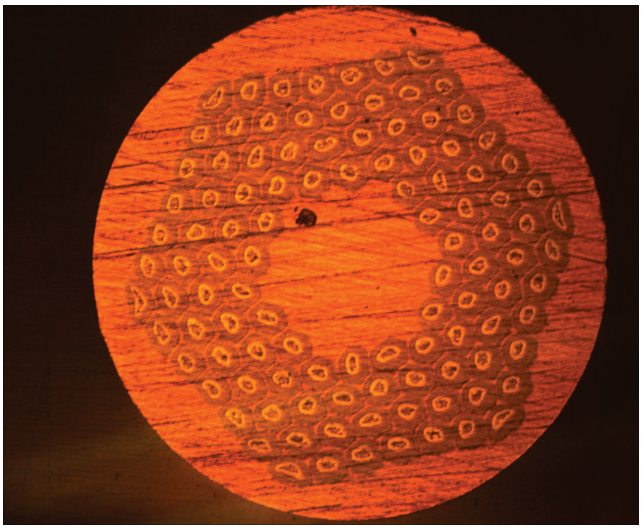

Figure 6.12: Cross Section of a 108/127 RRP Strand.

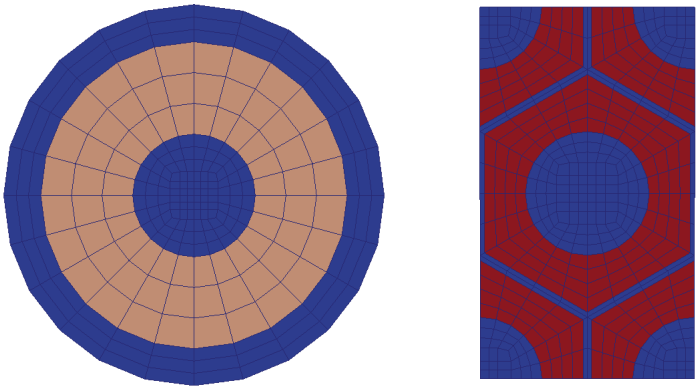

Figure 6.13: Mesh of Macroscale and RVE.

## 6.6 Test Case 3: Cooldown from 480 K to 4.2 K

This strand differs from the previous example in that it contains a copper core in the center of the strand, meaning that the stress state will vary throughout the homogenized region. To determine the material tangent at every integration point in the macrostructure, a finite element problem must be solved over the RVE at each of these points. Due to the large computational costs associated with these solutions, the axisymmetric geometry of the strand is exploited. Instead of solving for the material tangent at every integration point, the tangent is instead determine at three equally spaced radial points within the homogenized region, and linear interpolation is used to find the tangent elsewhere.

### 6.6.1 Results

Due to the nonlinearity present in the model, loading steps are taken in 10 K increments in order to aid convergence. The axial strain and axial stress of the homogenized strand at 4.2 K can be seen in figure 6.14, and the strain in the outer copper ring as a function of temperature can be seen in figure 6.15.

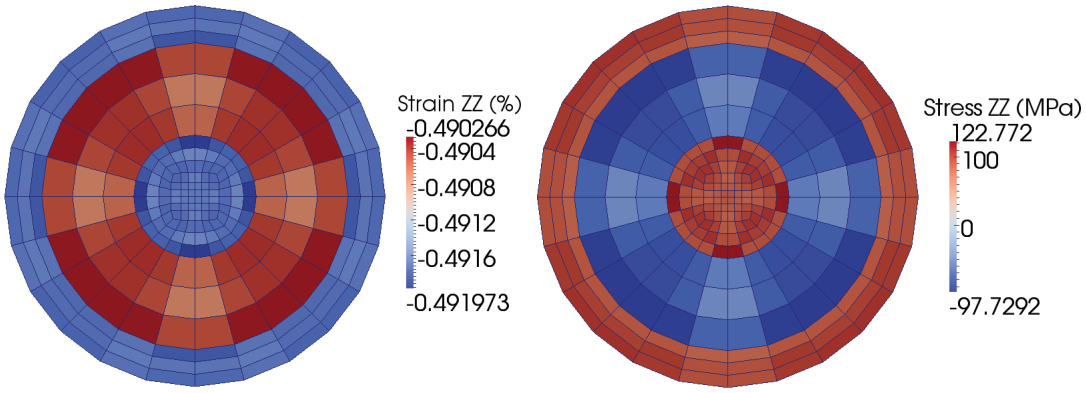


Figure 6.14: Axial Strain and Stress of a Homogenized Strand at 4.2 K.

Again, it can be seen that even though the geometry is axisymmetric, the use of a non-isotropic PUC introduces slight orthotropy into the solution. These errors can be addrssed by either using a higher penalty parameter (at the risk of creating an ill-conditioned stiffness matrix) when enforcing periodic boundary conditions, or by imposing the periodic contraints via Langrian methods. Furthermore, it is observed that the strain in the radial direction is larger than in the axial direction, indicating that during cooldown, transverse dimension changes in the strand have more impact than axial changes.

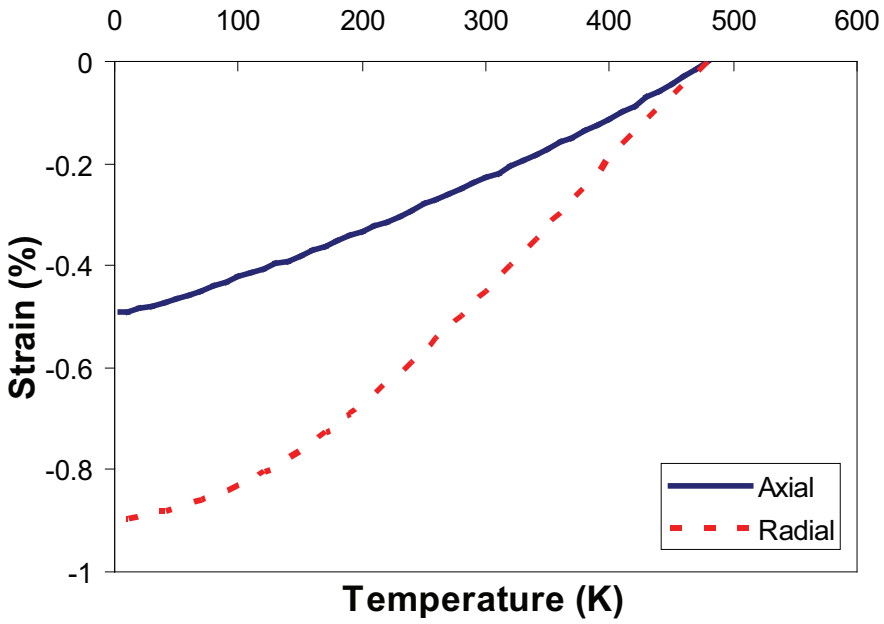


Figure 6.15: Strain in Outer Copper Ring.

It can be seen that the strand contracts by approximately half a percent simply by cooling it down to operating temperature. The copepr experiences a maximum tensile axial stress of 123 MPa, whereas the homogenized material experiences a maximum compressive stress of 98 MPa. This makes sense because since the strand is approximately 45 % Cu, the homogenized superconductor experiences less of an axial load to maintain equilibrium.

Due to the non-uniform deformation of the macrostructure, the solution over the RVE is dependent on its location within the strand. Therefore, the solution over the innermost and outermost RVEs within the homogenized region of the strand will be examined, labeled RVE 1 and RVE 2 respectively.

Figure 6.16 shows the elastic strain at 4.2 K at the RVE level. It can bee seen that the axial elastic strain in the $Nb_3Sn$ is similar in the inner and outer RVEs at approximately -0.16 %. However, the axial stress in the $Nb_3Sn$ differs between the two RVEs by approximately 34 MPa, as shown in figure 6.17. This behavior can be seen in thick-walled pressure vessels, where stress decreases in the radial direction.

Plots of the plastic strain in the RVE are shown in figure 6.18. The outer RVE exhibits higher maximum plastic strains than the inner RVE, at approximately 0.13 %, but since the volume over which plasticity occurs is small, the effects of plasticity between the subelements are small.

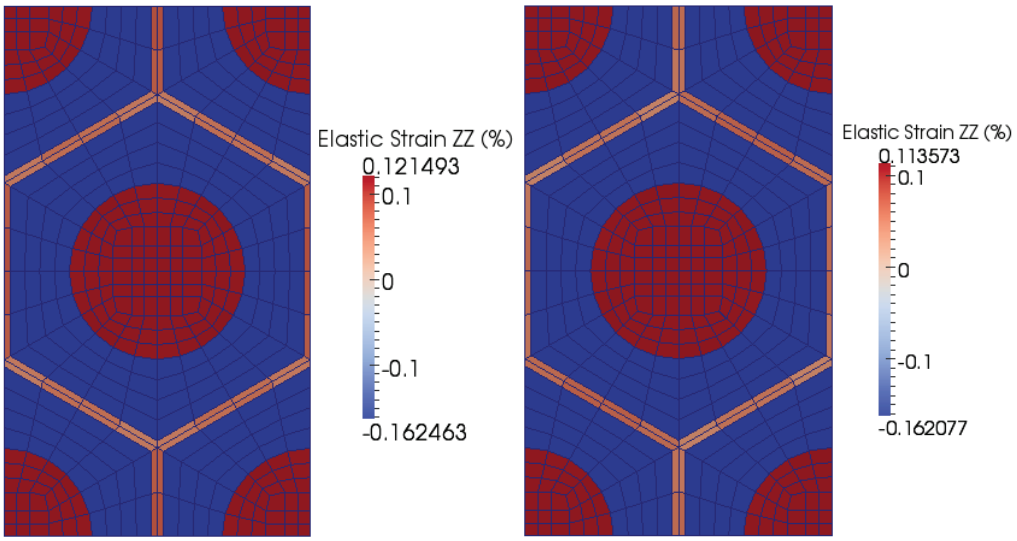


Figure 6.16: Axial Elastic Strain in RVE1 and RVE2 at 4.2 K, Respectively.

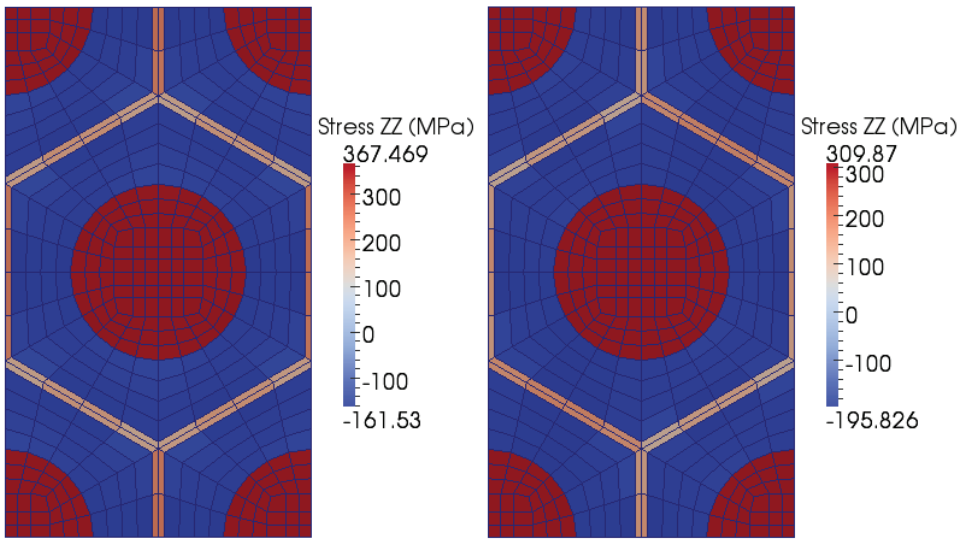


Figure 6.17: Axial Stress in RVE1 and RVE2 at 4.2 K, Respectively.

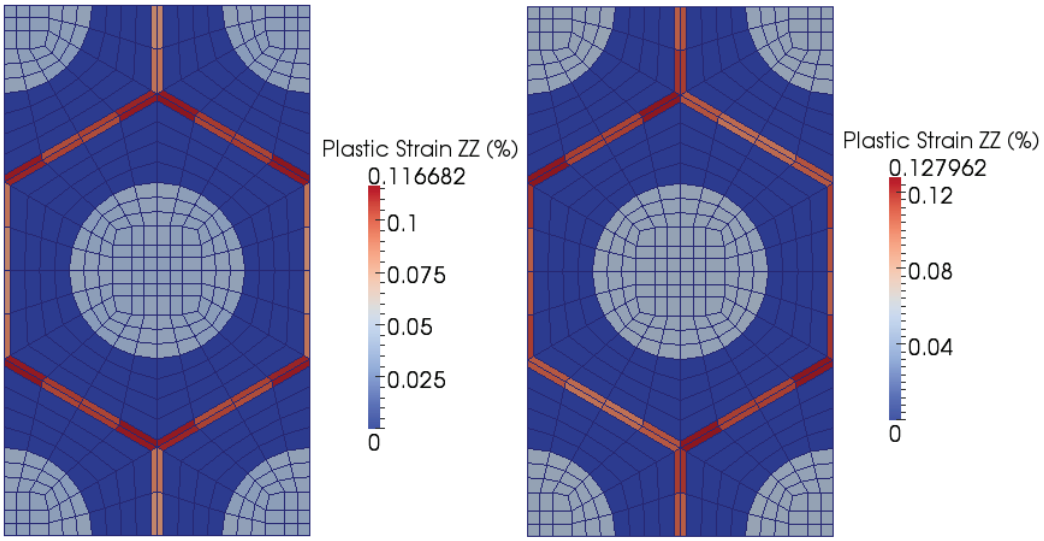


Figure 6.18: Axial Plastic Strain in RVE1 and RVE2 at 4.2 K, Respectively.

# Chapter 7

# Concluding Remarks

In this work, a multiscale model for superconducting accelerator magnets was developed. The model accounts for nonlinear effects, such as plasticity, as well as temperature dependence. The link between various lengthscales present within an accelerator magnet was established through homogenization techniques, and the determination of the effective properties of an RVE was performed by developing a nonlinear finite element code. Two treatments of the macroscale were implemented; the first being an approximation of the strand to a thin walled pressure vessel and the second being a finite element discritization. Simulations were performed on a strand in order to study the strain effects of cooling a magnet to an operation temperature of 4.2 K.

It was observed that the location to start the simulation is critical, as assuming a stress free configuration at 300 K versus 480 K gave a large discrepency between the strain states within the $Nb_3Sn$ phase. Additionaly, it may be possible that after the reaction of wires and cables, there is no stress free configuration, in which case a model of the reaction is required.

To address the introduction of orthotropy into the system through use of periodic boundary conditions, one can implement a hexogonal structure to the RVE, which behaves isotropically. Another possibility is to use other means of imposing the periodic constraints instead of penalty methods.

The inclusion of a copper core to the strand model increases the complexity of the model, requiring the effective properties of multiple filament RVEs to be computed every load step. Examination of the RVE behavior at the inner and outer portions of the homogenized region reveals that although the axial elastic strain is similar, other quantities such as axial stress don't match.

The addition of the cable scale into the multiscale model requires the strand to be treated as an RVE. However, if the RVE of the filament level behaves approximately linear, then it is possible to skip the strand scale and use the filament scale as an RVE to the cable.

Other considerations for future work include the necessity of a finitely deformed

Rutherford cable geometry, inclusion of voids and defects in the model, and a Sn distribution within the $Nb_3Sn$ phase.

# Bibliography


[1] J. Aboudi. *Mechanics of composite materials-a unified micromechanical approach*, volume 29. Elsevier, 1992.

[2] A. A. Abrikosov. *Zh. Eksperim. i Teor. Fiz.*, 43:1442, 1957.

[3] O. Axelsson. *Iterative Solution Methods*. Cambridge University Press, 1994.

[4] S. Geller B.T. Matthias, T.H. Geballe and E. Corenzwit. *Phys. Rev*, 95:1435, 1954.

[5] E. Buehler and H. J. Levinstein. Effect of tensile stress on the transition temperature and current-carrying capacity of $Nb_3Sn$. *J. Appl. Phys.*, 36(12):3856–3860, 1965.

[6] R.L. Burden and J. D. Faires. *Numerical Analysis*, volume 9. Brooks/Cole, 2011.

[7] P. Chadwick. *Continuum Mechanics-Concise Theory and Problems*. Dover Publications, Inc., 1999.

[8] G. Claudet and R. Aymar. Tore supra and he ii cooling of large high field magnets. *Adv. Cryog. Eng.*, 35:55–67, 1990.

[9] B. Collins. Introduction of nonlinear properties into hierarchical models of $Nb_3Sn$ strands. *IEEE Transactions on Applied Superconductivity*, 21:3:2320–2323, 2010.

[10] B.C. Collins, K. Matouš, and D. Rypl. Three-dimensional reconstruction of statistically optimal unit cells of multimodal particulate composites. *International Journal for Multiscale Computational Engineering*, 8:489–507, 2010.

[11] E. W. Collins. *Applied Superconductivity, Metallurgy and Physics of Titanium Alloys*. Plenum Press, New York, NY, 1986.

[12] M. Lefik D. Boso and B. Schrefler. A multilevel homogenized model for superconducting strands thermomechanics. *Cryogenics*, 45:4:259–71.

[13] M. Lefik D. Boso and B. Schrefler. Multiscale analysis of the influence of the triplet helicoidal geometry on the strain state of a $Nb_3Sn$ based strand for iter coils. *Cryogenics*, 45:9:589–605.

[14] P. F. Dahl. Superconductivity: Its historical roots and development from mercury to the ceramic oxides. *New York: American Institute of Physics*, page 13, 1992.

[15] W. Specking D.S. Easton, D.M. Kroeger and C.C. Koch. Prediction of the stress state in nb3sn superconducting composites. *J. Applied Phys.*, 51(5):2748–2757, 1980.

[16] H. T. Edwards. The tevatron energy doubler: a superconducting accelerator. *Ann. Rev. Nucl. Part. Sci.*, 35:605–660, 1985.

[17] J. W. Ekin. Strain effects in superconducting compounds. *Adv. Cryog. Eng. (Materials)*, 30:823–836, 1984.

[18] J.L. Ericksen. Magnetizable and polarizable materials. *Mathematics and Mechanics of Solids*, 13:38–54, 2008.

[19] A. Godeke et al. A general scaling relation for the critical current density in nb3sn. *Supercond. Sci. Techn.*, 19:R100–R116, 2006.

[20] Arbelaez et al. Cable deformation simulation and a hierarchical framework for $Nb_3Sn$ rutherford cables. *J. Phys.: Conf. Ser.*, 234, 2010.

[21] J.F. Bussière et al. Effects of ternary additions on young's modules and the martensitic transformation of nb3sn. *Adv. Cryog. Eng.*, 28:453, 1982.

[22] J.F. Bussière et al. Elastic behaviour of polycrstalline nb3sn v3ga and nb3ge. *Adv. Cryog. Eng.*, 30:859, 1983.

[23] Y. C. Fung. *A First Course in Continuum Mechanics*, volume 3. Prentice-Hall, 1994.

[24] U. Galvanetto and M. H. Ferri Aliabadi. *Multiscale Modeling in Solid Mechanics-Computational Approaches*, volume 3. Imperial College Press, 2010.

[25] A.E. Green and P.M. Naghdi. A general theory of an elastic-plastic continuum. *Archive for Rational Mechanics and Analysis*, 18:251–281, 1965.

[26] A.E. Green and P.M. Naghdi. A thermodynamic development of elastic-plastic continua. *Proceedings of IUTAM Symposium*, 1966.

[27] E. Gregory. Conventional wire and cable technology. *American Institute of Physics*, 249(2):1198–1229, 1992.

[28] The LHC Study Group. The large hadron collider. *CERN/AC/95-05 (LHC)*, 1995.

[29] V. Guritanu, W. Goldacker, Y. Wang F. Bouquet, R. Lortz, G. Goll, and A. Junod. Specific heat of nb3sn: The case for a second energy gap. *Phys. Rev. B*, 70(18):184526, 2004.

[30] M. Gurtin. The linear theory of elasticity. *Handbuch der Physik*, 1a/2, 1972.

[31] M. E. Gurtin. *An Introduction to Continuum Mechanics*, volume 158. Academic Press, 2003.

[32] Z. Hashin and S. Strikman. On some variational principles in anisotropic and non-homogeneous elasticity. *Journal of the Mechanics and Physics of Solids*, 10:335–342, 1962.

[33] Z. Hashin and S. Strikman. A variational approach to the theory of the elastic behaviour of multiphase materials. *Journal of the Mechanics and Physics of Solids*, 11:127–140, 1963.

[34] D. G. Hawksworth and D. C. Larbalestier. Enhanced value of $h_{C2}$ in nb-ti ternary and quaternary alloys. *Adv. Cryog. Eng. (Materials)*, 26:479–486, 1980.

[35] R. Hill. The elastic behaviour of a crystalline aggregate. *Proceedings of the Physical Society*, A65:349–354, 1952.

[36] R. Hill. Elastic properties of reinforced solids - some theoretical principles. *Journal of the Mechanics of Physics and Solids*, 11:357–372, 1963.

[37] T.J.R. Hughes. Numerical implementation of constitutive models: Rate independent deviatoric plasticity. *Theoretical Foundations for Large Scale Computations of Nonlinear Material Behavior*, 1984.

[38] T.J.R. Hughes. *The Finite Element Method-Linear Static and Dynamic Finite Element Analysis*. Dover Publications, Inc., 2000.

[39] N. Ida. *Engineering Electromagnetics*, volume 2. Springer, 2004.

[40] A. Iserles. *A first course in the numerical analysis of differntial equations*, volume 2. Cambridge University Press, 2009.

[41] K. Han J. Chen and P. Kalu. 3d stress-strain model of the $Nb_3Sn$ wire. *IEEE Transactions on Applied Superconductivity*, 21:3, 2011.

[42] C.A.M. van Beijnen J.D. Elen and C.A.M van der Klein. *IEEE Trans. Mag.*, 13:470, 1977.

[43] Y.B. Kim, C.F. Hempstead, and A.R. Strnad. Flux flow resistance in type-ii superconductors. *Phys. Rev. Lett.*, 139:A1163, 1962.

[44] S.V. Kochevets. Random sphere packing model of heterogeneous propellants. *PhD thesis, University of Illinois at Urbana-Champaign*, 2002.

[45] A. Kovetz. *Electromagnetic Theory*. Oxford University Press, 2000.

[46] H. Krauth. *Handbook of Applied Superconductivity*, volume 1, chapter Conductors for d.c. applications, pages 399–400. Taylor and Francis, 1998.

[47] P. J. Lee and D. C. Larbalestier. Development of nanometer scale structures in composites of nb-ti and their effect on the superconducting critical current densities. *Acta Metall*, 35(10):2523–2356, 1987.

[48] P. J. Lee, D. C. Larbalestier, K. Togano, K. Tachikawa, M. Suzuki, K. Hamasai, K. Noto, and K. Watanabe. *Composite Superconductors*. Marcel Dekker, Inc., 1994.

[49] M. S. Livingston and J. Blewett. *Particle Accelerators*. McGraw-Hill., 1962.

[50] D.G. Luenberger. *Linear and Nonlinear Programming*. Addison-Wesley Publishing Company, 1984.

[51] L. E. Malvern. *Introduction to the Mechanics of a Continuous Medium*. Prentice-Hall, 1969.

[52] J. E. Marsden and T. J. R. Hughes. *Mathematical Foundations of Elasticity*. Dover Publications, Inc., 1983.

[53] C. Meingast and D. C. Larbalestier. Quantitiative description of a very high critical current density nbti superconductor during its final optimization strain. *Journal of Applied Phyiscs*, 66(12):5971–5983, 1989.

[54] K. H. Mess, P. Schmüser, and S. Wolff. *Superconducting Accelerator Magnets*. World Scientific, 1996.

[55] N. Mitchell. Finite element simulations of elasto-plastic processes in nb3sn strands. *Cryogenics*, 45(7):501–515, 2005.

[56] G. Morrow. Progress in mri magnets. *IEEE Trans. Appl. Supercond.*, 10(1):744–751, 2000.

[57] C. B. Müller and E. J Saur. Influence of the mechanical constraints on the superconducting transition of $Nb_3Sn$-coated niobium wires and ribbons. *Adv. Cryog. Eng.*, 8:574–578, 1962.

[58] T. Mura. *Micromechanics of defects in solids*, volume 2. Kluwer Academic Publishers, 1993.

[59] S. Nemat-Nasser and M. Hori. *Micromechanics: overall properties of heteroegenous solids*, volume 2. Elsevier, 1999.

[60] E.S. Drexler N.J. Simon and R.P. Reed. Properties of copper and copper alloys at cryogenic temperatures. *NIST Monograph*, page 177, 1992.

[61] R.L. Taylor O.C Zienkiewicz and J.Z. Zhu. *The Finite Element Method-Its Basis and Fundamentals*, volume 6. Elsevier, 2005.

[62] J.T. Oden. *Finite Elements of Nonlinear Continua*. Dover Publications, Inc., 2000.

[63] H. Kamerlingh Onnes. *Leiden Commun.*, 124C, 1911.

[64] H. Kamerlingh Onnes. *Leiden Commun.*, 140B, 1914.

[65] T. P. Orlando, E. J. McNiff, S. Foner, and M. R. Beasley. Critical fields, pauli paramagnetic limiting, and material parameters of nb3sn and v3si. *Phys. Rev. B*, 19(9):45454561, 1979.

[66] E. M. Purcell and D. J. Morin. *Electricity and Magnetism*, volume 3. Cambridge University Press, 2013.

[67] E. F. Koch R. M. Scanlan, W. A. Fietz. Flux pinning centers in superconducting $Nb_3Sn$. *J. Appl. Phys.*, 46(5):2244–2249, 1975.

[68] A. Reuss. Berechnung der fliessgrenze von mischkristallen auf grund der plastizitätsbedingung für einkristalle. *Z. angew. Math. Mech.*, 9:49–58, 1929.

[69] J.M. Royet and R.M. Scanlan. Manufacture of keystoned flat superconducting cables for use in ssc dipoles. *IEEE Trans. Mag.*, 23:480–483, 1987.

[70] J.C. Simo and T.J.R. Hughes. *Computational Inelasticity*, volume 7. Springer, 1994.

[71] J.C. Simo and R.L. Taylor. Consistent tangent operators for rate-independent elastoplasticity. *Computer Methods in Applied Mechanics and Engineering*, 48:101–118, 1985.

[72] I.S. Sokolnikoff. *Mathematical Theory of Elasticity*, volume 2. McGraw-Hill, 1956.

[73] D.J. Steigmann. On the formulation of balance laws for electromagnetic continua. *Mathematics and Mechanics of Solids*, 14:390–402, 2009.

[74] D.R.S. Talbot and J.R. Willis. Variational priniciples for inhomogeneous nonlinear media. *IMA J. Appl. Math.*, 35:39–54, 1985.

[75] D.B. Thomas and M.N. Wilson. Filamentary superconductors for pulsed magnets. *Proc. of 4th Int. Conf. on Magnet Tech.*, 48:493–497, 1972.

[76] S. Timoshenko and J.N. Goodier. *Theory of Elasticity*, volume 3. McGraw-Hill, 1969.

[77] S. Torquato. Random heterogeneous media: microstructure and improved bounds on effective properties. *Applied Mechanics Review*, 44:37–76, 1991.

[78] S. Torquato. Effective stiffness tensor of composite media i. exact series expansions. *Journal of the Mechanics and Physics of Solids*, 45:1421–1448, 1997.

[79] S. Torquato. Effective stiffness tensor of composite media ii. applications to isotropic dispersions. *Journal of the Mechanics and Physics of Solids*, 46:1411–1440, 1998.

[80] S. Torquato. *Random Heterogeneous Materials: Microstructure and Macroscopic Properties*. Springer-Verlag, 2002.

[81] S. Torquato and S. Hyun. Effective-medium approximation for composite media: Realizable single-scale dispersions. *Journal of Applied Physics*, 89:1725–1729, 2001.

[82] B. Turck. Tore supra: a tokamak with superconducting toroidal field coils; status report after the first plasmas. *IEEE Trans. Magn.*, 25(2):1473–1480, 1989.

[83] W. Voigt. Über die beziehung zwischen den beiden elastizitätskonstanten isotroper körper. *Wied. Ann. Physik*, 38:573–587, 1889.

[84] M. N. Wilson. *Superconducting Magnets*. Clarendon Press, Oxford, UK, 1983.

[85] M. N. Wilson. Superconducting materials for magnets. *CERN/96-03*, pages 47–69, 1996.

[86] K. Yoshizaki Y. Hashimoto and M. Tanaka. *Proc. 5th International Cryogenic Eng. Conf.*, page 332, 1974.

[87] Y. Yang and E. Martínez. Ac losses in conductors. *Handbook of Superconducting Materials*, 2:1398–1401, 2002.

[88] R.E. Taylor Y.S. Touloukian, R.K. Kirby and P.D. Desai. *Thermophysical properties of matter. Metallic elements and alloys*, volume 12. Plenum Publishing Co., 1975.

[89] T.I. Zohdi. *Electromagnetic Properties of Multiphase Dielectrics-A Primer on Modeling, Theory and Computation*. Springer, 2012.

[90] T.I. Zohdi and P. Wriggers. *Lecture Notes in Applied and Computational Mechanics*, volume 20. Springer, 2008.